Crystallochromy of perylene pigments: Interference between Frenkel excitons and charge-transfer states

Linus Gisslén[*] and Reinhard Scholz[†]

Physik Department und Walter Schottky Institut, Technische Universität München, Am Coulombwall 3, D-85748 Garching, Germany

The optical properties of perylene-based pigments are arising from the interplay between neutral molecular excitations and charge transfer between adjacent molecules. In the crystalline phase, these excitations are coupled via electron and hole transfer, two quantities relating directly to the width of the conduction and valence band in the crystalline phase. Based on the crystal structure determined by x-ray diffraction, density-functional theory (DFT) and Hartree-Fock are used for the calculation of the electronic states of a dimer of stacked molecules. The resulting transfer parameters for electron and hole are used in an exciton model for the coupling between Frenkel excitons and charge-transfer states. The deformation of the positively or negatively charged molecular ions with respect to the neutral ground state is calculated with DFT and the geometry in the optically excited state is deduced from time-dependent DFT and constrained DFT. All of these deformations are interpreted in terms of the elongation of an effective internal vibration which is used subsequently in the exciton model for the crystalline phase. A comparison between the calculated dielectric function and the observed optical spectra allows to deduce the relative energetic position of Frenkel excitons and the charge-transfer state involving stack neighbors, a key parameter for various electronic and optoelectronic device applications. For five out of six perylene pigments studied in the present work, this exciton model results in excellent agreement between calculated and observed optical properties.

I. INTRODUCTION

Due to their vivid colors and their long-term chemical stability, various perylene-based pigments have found applications as high quality varnish with an excellent light fastness.[1,2] Moreover, the semiconducting properties of these materials have resulted in device applications including field effect transistors,[3] sensors,[4] photovoltaic applications,[5] erasable optical disks,[6] xerographic photoreceptors,[7] and hole-conducting layers in light-emitting diodes.[8]

In solution, several of these chromophores show similar absorption spectra, with clear evidence for a strong coupling between internal vibrations and optical excitation.[9–12] The large variation between the optical properties of the corresponding molecular crystals demonstrates that the influence of the side groups on the geometric arrangement of adjacent molecules has a strong influence on intermolecular interactions, defining eventually a specific color shade of each pigment. The attempts to relate the color of perylene diimides to the geometry in the crystalline phase have started from purely phenomenological parametrizations.[13] In simplified model geometries for stacked molecules, the size and sign of electron and hole transfer were calculated determining in turn the width of the conduction and valence band, respectively.[14] However, as the optical properties depend mainly on neutral molecular excitations and their transfer between adjacent molecules,[15] the relation between the transfer of charges and the spectroscopic observables has still remained unclear.

The influence of the mixing between neutral molecular excitations and charge-transfer (CT) states on the absorption spectra was first recognized in exciton models for dimers[16,17] and one-dimensional stacks.[18,19] For PTCDA (3,4,9,10-perylene tetracarboxylic dianhydride), the exciton transfer between different basis molecules of the crystal lattice results in different shapes of the diagonal elements of the dielectric function,[20,21] in qualitative agreement with ellipsometry data obtained on single crystals.[22] The influence of Frenkel (F) and CT states on the electroabsorption of this material was investigated in a simplified F-CT model,[23] but the approach used did not take into account the redistribution of oscillator strength between different vibronic sublevels of the Frenkel exciton manifold, a phenomenon required to fulfill elementary sum rules.[24–26] Based on a more sophisticated approach to the deformation of excited or charged molecules, it was found that a theoretical analysis of the optical spectra obtained on Me-PTCDI (N,N′-dimethyl-3,4,9,10-perylenetetracarboxylic diimide) requires a mixing between Frenkel and CT states.[19] For PTCDA, on the other hand, Frenkel excitons and CT states result in independent photoluminescence (PL) features,[27] where the interpretation of PL from CT states requires the investigation of self-trapped CT excitons in deformed dimer geometries.[28] A model including only Frenkel excitons has allowed to quantify the anisotropic dielectric tensor, PL at low temperatures, and the dependence of electron-energy-loss spectra on the momentum transfer.[20–22,29–31]

Previous microscopic calculations of dielectric function and PL spectra raise the fundamental question under which conditions separate F and CT states or their mixing via electron or hole transfer determine the optical observables. In the following, we extend a Frenkel-CT approach developed earlier for a one-dimensional stack to a crystal model accounting for both basis molecules in the unit cell, combining two key ingredients applied earlier to the calculation of the anisotropic optical response of perylene compounds.[18–21] The deformation of each molecule in its anionic, cationic, and optically excited states is deduced from DFT calculations,

parametrized in terms of the elongation of an effective internal vibration. DFT and Hartree-Fock (HF) calculations applied to a pair of stacked molecules reveal intermolecular parameters such as electron transfer and hole transfer. In such a stacked dimer, the transition dipole between the electronic ground state and the CT state and the transition dipole of neutral molecular excitations can be derived from DFT and time-dependent DFT (TD-DFT) calculations. The transfer of a neutral molecular excitation toward different sites is constrained by a sum rule relating the center of mass of the absorption band to the molecular deformation and excitation transfer, so that the required transfer parameter can be deduced in a controlled way from the observed spectra.[24–26] Based on these constraints for the quantities entering the exciton model, we use the energies of neutral excitations and CT states as the only free parameters. Our approach is limited to transitions arising from the highest molecular orbital (HOMO) and lowest occupied molecular orbitals (LUMO). For diindeno-perylene, higher transitions and the respective CT states seem to have a minor influence on the lowest absorption band,[32] but for the other perylene compounds investigated in the present work, we found little evidence for a similar phenomenon.

In Sec. II we describe the perylene compounds studied in this work including calculations of their deformation patterns and a comparison between observed and calculated vibronic progressions. Based on an analysis of the crystal geometry, Sec. III discusses DFT and Hartree-Fock calculations for dimers of stacked molecules yielding *ab initio* assignments for electron transfer, hole transfer, and the transition dipole toward the CT state. Section IV presents the exciton model applied in Secs. VII and VIII to calculations of the dielectric function and the complex refractive index. For all perylene compounds, we use molecular and intermolecular parameters derived from DFT or Hartree-Fock, but we adjust the calculated line shapes to the observed spectra by varying the energies of neutral molecular excitations and CT states. The energetic difference between these two types of crystal excitations turns out to have a sensitive influence on the shape of the optical response. Therefore, our calculations allow deriving this key parameter for optoelectronic device applications directly from the observed spectra. The main achievements of this work are summarized in Sec. IX.

II. PERYLENE COMPOUNDS STUDIED IN PRESENT WORK

In order to validate our exciton model, we apply it to six different molecular crystals: PTCDA, also known as red pigment PR224, Me-PTCDI (red pigment PR179), N,N'-bis(3,5-xylyl) perylene-3,4,9,10-bis(dicarboximide) (red pigment PR149), N,N'-bis(2-phenylethyl)perylene-3,4,9,10-bis(dicarboximide) (black pigment PB31), 3,4,9,10-perylene-bis(dicarboximide) (PTCDI, violet pigment PV29) and diindenoperylene (DIP), compare Fig. 1. In the following, the names of two of these molecules will be abbreviated by their pigment names PB31 and PR149.

All molecules except for DIP share similar geometric features: a perylene core surrounded by four carboxylic groups
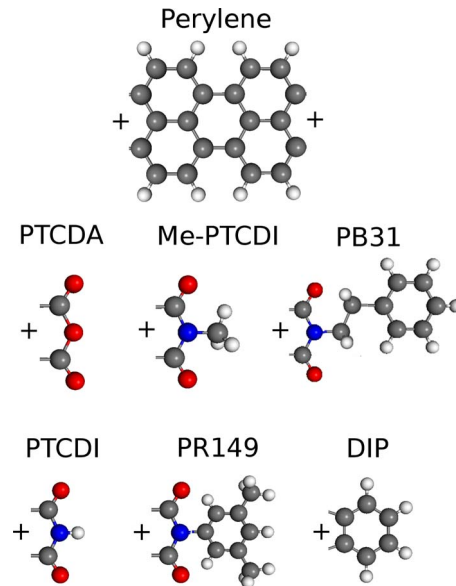
FIG. 1. (Color online) Compounds studied in the present work consisting each of a perylene core and two identical end groups surrounding the core. Upper row: PTCDA, Me-PTCDI, PB31 [N,N'-bis(2-phenylethyl)perylene-3, 4, 9, 10-bis(dicarboximide)], lower row: PTCDI, PR149 [N,N'-bis(3,5-xylyl)perylene-3,4,9,10-bis(dicarboximide)], and DIP, as annotated.

and two identical functional groups consisting of oxygen (PTCDA) or of an imide group with a side group of varying size, ranging from hydrogen (PTCDI) toward -CH_2-CH_2-phenyl (PB31). In all cases, both HOMO and LUMO have a node plane along the long axis so that the size of the functional group has only a marginal influence on the optical properties of the respective chromophore; compare Fig. 2 for the frontier orbitals of Me-PTCDI. In DIP, on the other hand, the planar aromatic region is completed by two indeno groups so that both HOMO and LUMO spread over the entire molecular plane.[32] Nevertheless, this larger extension of the frontier orbitals does not result in a substantial redshift with respect to the other perylene compounds.

A. Spectroscopic features of dissolved chromophores

In this section, we analyze published absorption spectra of five out of the six model compounds obtained at low concentrations in different solvents.[11,12,32] As long as the concentration of the dissolved chromophores is sufficiently low, a significant influence of aggregation on the observed spectra can be excluded, with the possible exception of PTCDA.[9,12] The distinct subbands of the absorption spectra are assigned to a progression over an effective internal vibration with energy $\hbar\omega$. For a single molecule, the normalized transition probability P_n from the lowest vibrational level $|0_g\rangle$ in the electronic ground state toward the nth vibronic level $|n_e\rangle$ in the excited potential is given by a Poisson progression determined by the effective Huang-Rhys factor S,

$$P_n(S) = e^{-S}\frac{S^n}{n!}. \tag{1}$$

The contribution of each sublevel to the dielectric function of a dilute solution is modeled by a normalized Gaussian,
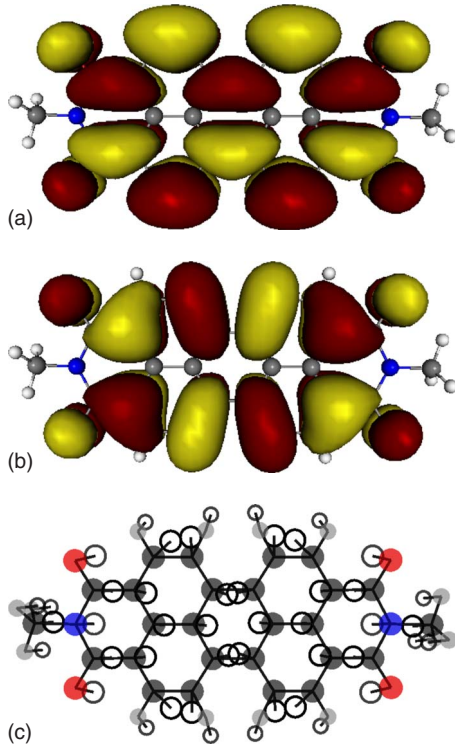
FIG. 2. (Color online) LUMO (top) and HOMO (middle) of Me-PTCDI. Bottom: deformation in the relaxed excited geometry (open circles, deformation increased by a factor of 30), together with the geometry in the electronic ground state (solid circles). The relaxed excited geometry underlying this visualization has been calculated with the constraint $n_{\text{HOMO}}=n_{\text{LUMO}}=1$ at the B3LYP/TZ level.

$$\Im[\varepsilon(E)] = A \sum_n P_n(S) \frac{1}{\sigma_n\sqrt{\pi}} \exp\left(-\frac{(E-E_{0n})^2}{\sigma_n^2}\right). \quad (2)$$

At low concentration, the influence of the dissolved chromophores on the refractive index of the solution is very small, so that the observed absorption coefficient can be obtained as

$$\alpha(E) = \frac{E}{\hbar c} \frac{\Im[\varepsilon(E)]}{n_{\text{solvent}}}. \quad (3)$$

The fitting procedure gives vibronic subbands which are approximately equally spaced, $E_{0n} \approx E_{00}+n\hbar\omega$, and the effective mode reported in Table I is defined as $\hbar\omega = (E_{02} - E_{00})/2$. The fits of the observed spectra demonstrate that the side groups have only a marginal influence on the optical response; compare Table I.

B. Optimization of molecular geometry in different electronic configurations

In the following, all calculations of molecular properties are performed with the B3LYP three parameter hybrid functional[33] because this approach gives excellent agreement with observed molecular geometries and measured frequencies of vibrational modes.[34,35] For investigations of a single molecule, we use a well converged triple-ζ (TZ) variational basis for the electronic orbitals.[36] DFT calculations for the electronic ground state and TD-DFT optimizations of the relaxed excited geometry have been performed with the respective routines implemented in the TURBOMOLE 5.7 program package.[37–39] From a comparison with the observed spectra in Table I, we found that an optimization of the excited state geometry with the constraint $n_{\text{HOMO}}=n_{\text{LUMO}}=1$ is more reliable than the geometry obtained with TD-DFT. As the excited state with this modified electronic configuration is the ground state of the corresponding symmetry, this way of using DFT is covered by the Hohenberg-Kohn theorem.[40] In our model compounds, the lowest optical transition is always dominated by the HOMO-LUMO excitation, so that constrained DFT and TD-DFT are expected to be equivalent. Indeed, both approaches yield similar deformation patterns in the relaxed excited geometry, but in all cases the deformation deduced from TD-DFT is significantly smaller. The geometry of positively and negatively charged ionized molecules is obtained with DFT. Each charged or excited state conserves the molecular symmetry, so that the point group remains the same as in the electronic ground state, i.e., D_{2h} for PTCDA, PTCDI and DIP, or C_{2h} for the other compounds.

TABLE I. Comparison between observed solution spectra, constrained DFT (c-DFT) calculations of the deformation pattern in the relaxed excited state, and time-dependent DFT (TD-DFT) calculations of this deformation pattern. The experimental spectra are fitted to a Poisson progression for the dielectric response with argument S and vibronic spacing $\hbar\omega$, compare Eqs. (1)–(3), and in the two types of DFT calculations, the effective mode $\hbar\omega$ and its Huang-Rhys parameter S are defined via Eqs. (5) and (6).

	E_{00}	S	$\hbar\omega$	S	$\hbar\omega$	S	$\hbar\omega$
Compound	Solution spectra			c-DFT		TD-DFT	
PTCDA (Ref. 12)	2.363	0.86	0.172	0.88	0.171	0.56	0.171
Me-PTCDI (Ref. 12)	2.363	0.80	0.173	0.87	0.170	0.56	0.171
PB31 (Ref. 11)	2.350	0.80	0.169	0.87	0.170	0.56	0.171
PTCDI				0.82	0.175	0.51	0.176
PR149 (Ref. 11)	2.360	0.84	0.170	0.88	0.170	0.53	0.171
DIP (Ref. 32)	2.351	0.87	0.167	0.93	0.165	0.64	0.170

C. Vibronic coupling constants and Huang-Rhys factors for internal vibrations

The vibrational modes in the electronic ground state of each molecule are calculated with B3LYP/TZ. The deformation patterns for anionic, cationic, and excited molecules are projected onto the complete set of vibrational eigenvectors giving in each case the vibronic coupling constants. An elongation of an internal vibration with energy $\hbar\omega_k$ can only occur for breathing modes with A_g symmetry, resulting in a reorganization energy λ_k of each mode defining its Huang-Rhys factor,

$$\lambda_k = S_k \hbar\omega_k, \quad (4)$$

where the latter is sometimes expressed in terms of the vibronic coupling constant g_k as $S_k = g_k^2$. For each vibration, S_k defines a Poisson progression for its contribution to the optical spectra, compare Eq. (1), and the intensities of mixed harmonics of different modes are given by the product of the respective transition probabilities $P_n(S_k)$. For the mode frequencies, we apply a scaling factor of 0.973 adequate for the B3LYP functional,[35] but we conserve the reorganization energies λ_k deduced from the potential energy surface, so that the Huang-Rhys factors S_k are increased by a factor of 1/0.973. As an example, Table II reports the internal vibrations of PTCDA together with the Huang-Rhys factors S_k^- for the molecular anion, S_k^+ for the cation, and S_k for the excited molecule. In the latter case, we compare the deformation pattern obtained under the constraint $n_{HOMO} = n_{LUMO} = 1$ with the results of TD-DFT, giving in both cases a set of mode elongations compatible with the relative size of the cross sections observed in resonant Raman spectra.[41,42] The Huang-Rhys factors related to neutral excitation of the model compounds are visualized in Fig. 3, and for PTCDA, PTCDI, and Me-PTCDI, the mode frequencies and Huang-Rhys factors are compatible with observed resonant Raman cross sections.[41–44]

D. Effective vibrational mode

In the observed spectra of dissolved chromophores, the various internal vibrations are not resolved, but due to the large Gaussian broadening arising from a fluctuating shell of surrounding solvent molecules, they merge into a single vibronic progression. Therefore, we compress the detailed information obtained from the projection of the deformation patterns onto the vibrational eigenvectors into an effective mode with an effective Huang-Rhys factor,

$$S = \sum_k S_k, \quad (5)$$

$$\hbar\omega = \frac{1}{S} \sum_k S_k \hbar\omega_k, \quad (6)$$

where the sums are calculated over the range 900–1800 cm^{-1}. As the deformation patterns of ionized and excited states are qualitatively similar, the energies of the effective modes deduced from the different deformation patterns deviate only by a few percent. Nevertheless, the effec-

TABLE II. Vibronic A_g modes in the electronic ground state of PTCDA, obtained at the B3LYP/TZ level, with frequencies scaled by a factor of 0.973. The Huang-Rhys factors are derived from the geometries of ionized molecules or from the lowest excited state. In the latter case, we compare the results derived from a geometry of the relaxed excited state obtained under the constraint $n_{HOMO} = n_{LUMO} = 1$ (c-DFT) with the excited state geometry obtained from TD-DFT. In each case, the properties of an effective mode are calculated (last two lines, mode energy in cm^{-1}), averaged over the interval 900 to 1800 cm^{-1} according to Eqs. (5) and (6).

Mode	Cation	Anion	Excited c-DFT	Excited TD-DFT
$\hbar\omega_k$ cm^{-1}	S_k^+ 1	S_k^- 1	S_k 1	S_k 1
225	0.123	0.066	0.404	0.286
380	0.038	0.067	0.005	0.006
457	0.028	0.008	0.008	0.005
520	0.001	0.109	0.081	0.080
605	0.048	0.004	0.057	0.048
709	0.006	0.000	0.007	0.009
819	0.005	0.003	0.000	0.000
1013	0.042	0.001	0.026	0.014
1111	0.034	0.036	0.000	0.002
1232	0.005	0.059	0.022	0.013
1299	0.147	0.128	0.404	0.257
1325	0.002	0.039	0.020	0.017
1357	0.016	0.078	0.120	0.063
1423	0.010	0.016	0.032	0.020
1552	0.044	0.121	0.217	0.152
1567	0.001	0.084	0.038	0.024
1669	0.048	0.087	0.001	0.001
3096	0.000	0.000	0.000	0.000
3123	0.000	0.000	0.000	0.000
S	0.349	0.649	0.880	0.562
$\hbar\omega$	1335	1425	1376	1382

tive Huang-Rhys factors in Table II differ strongly because the deformations of the ionized molecules are significantly smaller. When comparing the effective Huang-Rhys factors for neutral excitation with the experimental results reported in Table I, it turns out that TD-DFT underestimates the deformation of the excited molecules substantially, as opposed to the constrained DFT calculation with $n_{HOMO} = n_{LUMO} = 1$, yielding good agreement with the observed intensity ratios of the vibronic subbands: The calculated Huang-Rhys factors are overestimated by less than 10% with respect to the values fitted to the observed spectra; compare Table I. Therefore, in the exciton model discussed in Sec. IV, the elongation of the effective mode will be parametrized according to the constrained DFT calculation. The calculated Huang-Rhys factors in the different charge states and in the relaxed excited geometry are summarized in Table III, with the energy of the effective mode according to the constrained DFT calculation of the excited state.
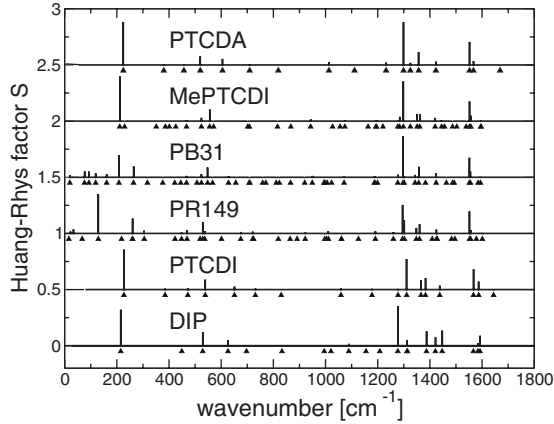
FIG. 3. Huang-Rhys factors for neutral excitation of the six perylene compounds, obtained at the B3LYP/TZ level under the constraint $n_{HOMO} = n_{LUMO} = 1$, with base lines shifted for clarity. All mode energies have been scaled by a factor of 0.973 adequate for the B3LYP functional (Ref. 35) and the Huang-Rhys factors by 1/0.973.

For the anionic and cationic coupling constants, information on perylene compounds are rather scarce. In all cases, we find that the reorganization energy of the positively charged ionized state is smaller than for the anionic state, and that the relaxed excited state is deformed even more, fulfilling $S_+ < S_- < S$ and the approximate sum rule $S_+ + S_- \approx S$. From earlier calculations for PTCDA, the resulting values $S_+ = 0.72$ and $S_- = 0.34$ have indicated the opposite behavior, $S_+ > S_-$.[23] In previous attempts to assign the spectra of PTCDA and Me-PTCDI with a Frenkel-CT model, both compounds were parametrized with $S = 0.77$ fitted to solution spectra, assuming that both ionized states are governed by half of this Huang-Rhys factor, $S_+ = S_- = S/2$.[19] Photoionization spectra of pentacene have been interpreted with DFT,[45] and as our computational scheme reproduces these results for the cationic state together with a larger deformation of the anionic molecule, we are confident that the B3LYP functional is well suited for ionized perylene compounds as well. In the exciton model discussed below, the deformations of the charged molecules and the deformation in the optically excited state will be parametrized according to the values in Table III.

TABLE III. Effective internal vibration for the six perylene compounds, with Huang-Rhys factors S_- and S_+ of the ionized states obtained with DFT, and the Huang-Rhys factor in the relaxed excited geometry with constrained DFT, all at the B3LYP/TZ level.

Compound	Mode $\hbar\omega$	Cation S_+	Anion S_-	Excited S
	eV	1	1	1
PTCDA	0.171	0.35	0.65	0.88
Me-PTCDI	0.170	0.34	0.62	0.87
PB31	0.170	0.17	0.64	0.87
PTCDI	0.175	0.28	0.55	0.82
PR149	0.170	0.19	0.73	0.88
DIP	0.165	0.31	0.56	0.93

III. CRYSTAL STRUCTURE OF PERYLENE PIGMENTS

A. Crystal geometry and dielectric response

In the crystalline phases of the various perylene compounds, the stacking geometry is determined by the Coulomb interaction between charged regions of the molecules, van der Waals attraction favoring a large geometric overlap of adjacent perylene cores, and the steric hindrance introduced by side groups of different size. For PTCDA and Me-PTCDI, the Coulomb attraction between the oppositely charged carbon and oxygen atoms in the carboxylic groups of stack neighbors plays a dominant role, so that the stacking vector remains rather close to the molecular normal. The pigments PR149 and PB31 realize the opposite limit because the large side groups enforce a strong deviation between the stacking direction and the normal of the molecular planes.

All six compounds have a monoclinic phase crystallizing in the space group $P2_1/c$ with two basis molecules in the crystal unit cell; compare Table IV. In the case of PTCDA, the present work will concentrate on the α phase because detailed optical investigations of the pure β phase are still lacking and x-ray characterizations of thin films prove that the α phase dominates.[46,51] PB31 and DIP can crystallize in a space group with four basis molecules,[6,47,50] but in order to demonstrate the transferability of our exciton model among compounds realizing the same space group, these more com-

TABLE IV. Crystal structures for the six model compounds ordered according to the length of the stacking vector (highlighted, **a** for all compounds except for PR149, where the stacking vector is **b**). In the monoclinic space group $P2_1/c$, the lattice vector **b** is orthogonal to the other two, $a \perp b \perp c$, β is the angle between the lattice vectors **a** and **c**, and V_0 is the volume of the unit cell.

Compound	Ref.	a (Å)	b (Å)	c (Å)	β (deg)	V_0 (Å³)
α-PTCDA	46	**3.72**0	11.960	17.340	98.80	762.4
Me-PTCDI	2	**3.874**	15.580	14.597	97.65	873.2
PB31	47	**4.737**	32.450	9.507	100.27	1438.0
PTCDI	48	**4.865**	14.660	10.844	91.33	773.2
PR149	49	17.030	**4.869**	17.096	93.40	1413.7
DIP	50	**7.171**	8.550	16.798	92.42	1039.0

TABLE V. Angle δ between the molecular HOMO-LUMO transition dipole and the lattice vector $\boldsymbol{b}$ and relative contributions of this transition to the strength of the dielectric response ϵ_{yy} along $y \parallel \boldsymbol{b}$ and to the component ϵ_{xx} with $x \parallel (\boldsymbol{\mu}_A - \boldsymbol{\mu}_B)/\sqrt{2}$.

Compound	δ deg	ϵ_{yy} $\cos^2 \delta$	ϵ_{xx} $\sin^2 \delta$
α-PTCDA	41.0	0.57	0.43
Me-PTCDI	18.4	0.90	0.10
PB31	53.1	0.36	0.64
PTCDI	81.5	0.02	0.98
PR149	83.7	0.01	0.99
DIP	88.5	7×10^{-4}	1.00

plicated cases will not be discussed in the following.

In the space group $P2_1/c$, the $\boldsymbol{b}$ lattice vector defines a C_2 axis followed by a shift of $(\mathbf{b}+\mathbf{c})/2$, with the important consequence that all second-order tensors decouple into a 1×1 block for this direction and a 2×2 block governing the plane spanned by the lattice vectors $\boldsymbol{a}$ and $\boldsymbol{c}$. The transition dipole of the HOMO-LUMO transition of each molecule is oriented along its long axis. In the following, we shall use the convention that the transition dipoles $\boldsymbol{\mu}_A$ and $\boldsymbol{\mu}_B$ of the two basis molecules form an angle below $90°$ with the $\boldsymbol{b}$ lattice vector, so that their sum $(\boldsymbol{\mu}_A + \boldsymbol{\mu}_B)/\sqrt{2}$ is oriented along $\boldsymbol{b}$, whereas the difference $(\boldsymbol{\mu}_A - \boldsymbol{\mu}_B)/\sqrt{2}$ is located in the ac plane. Discarding the small contributions of intermolecular transition dipoles toward CT states, this allows deducing the relative strength of the dielectric response along these orthogonal directions,

$$\int dE \mathfrak{I}[\epsilon_{yy}(E)] = \frac{2\pi}{\epsilon_0 V_0} \left(\frac{\boldsymbol{\mu}_A + \boldsymbol{\mu}_B}{\sqrt{2}} \right)^2, \qquad (7)$$

$$\int dE \mathfrak{I}[\epsilon_{xx}(E)] = \frac{2\pi}{\epsilon_0 V_0} \left(\frac{\boldsymbol{\mu}_A - \boldsymbol{\mu}_B}{\sqrt{2}} \right)^2, \qquad (8)$$

where ϵ_{yy} denotes the diagonal component of the dielectric tensor along $\boldsymbol{b}$ and ϵ_{xx} stands for the response along the direction defined by $(\boldsymbol{\mu}_A - \boldsymbol{\mu}_B)/\sqrt{2}$. The integration in Eqs. (7)

and (8) shall extend over an energetic range of about 1.8–3.2 eV covering the HOMO-LUMO transition in the crystalline phase. Due to the simple dependence of the dielectric response on the orientation of the molecular transition dipoles, the relative strengths can be expressed in terms of the angle δ between the molecular long axes and the $\boldsymbol{b}$ lattice vector in the form $\cos^2 \delta$ and $\sin^2 \delta$, respectively; compare Table V.

B. Geometric arrangement of stack neighbors

For five of the six model compounds, the stacking distance measured along the molecular normal remains close to the value of 3.35 Å for graphite; compare Table VI. In DIP, the transverse offset between stack neighbors is so large that their aromatic cores hardly overlap, and as a result, the distance measured along the molecular normal is much smaller, close to the sum of the van der Waals radii of carbon and hydrogen. In all cases, the stacking vector is much longer than the distance between the molecular planes producing substantial projections onto the long axis and the short axis of the molecule.

C. Electron and hole transfer along stacking direction

The stacking geometry determines the size and sign of the transfer parameters t_e for an electron and t_h for a hole. For simplified model geometries where the stacked molecules are displaced exclusively along the long axis or along the short axis, it turned out that the signs of these transfer parameters depend critically on the specific stack geometry.[14] However, as the crystal phases of the six model compounds realize a sliding both along the long axis and along the short axis, compare Table VI, the signs of the transfer parameters may differ from the simplified geometries used in this seminal work.

The values for the transfer parameters can be deduced from a DFT or HF calculation for a pair of stacked molecules in a geometry compatible with the crystalline phase. The pairs of frontier orbitals are governed by simple Hamiltonians such as

$$H_{\text{LUMO}} = \begin{pmatrix} E_{\text{L}} & t_{\text{L}} \\ t_{\text{L}} & E_{\text{L}} \end{pmatrix} \qquad (9)$$

with eigenstates defined by symmetric or antisymmetric superpositions of the molecular orbitals,

TABLE VI. Geometric arrangement of chromophores with respect to each other: lattice vector along the stacking direction and projections into the Cartesian reference frame of the molecule defined by its long axis, short axis, and molecular normal. Only for large angles φ between the long axes of the two basis molecules, the dielectric tensor has substantial contributions along two orthogonal directions; compare Table V.

Compound	Stack (Å)	Long (Å)	Short (Å)	Normal (Å)	φ (deg)
α-PTCDA	3.72	1.20	1.03	3.37	82.1
Me-PTCDI	3.874	0.89	1.52	3.45	36.8
PB31	4.737	3.16	0.74	3.45	73.7
PTCDI	4.865	3.38	1.10	3.32	17.1
PR149	4.869	0.54	3.38	3.46	12.7
DIP	7.171	2.42	6.03	3.02	3.1
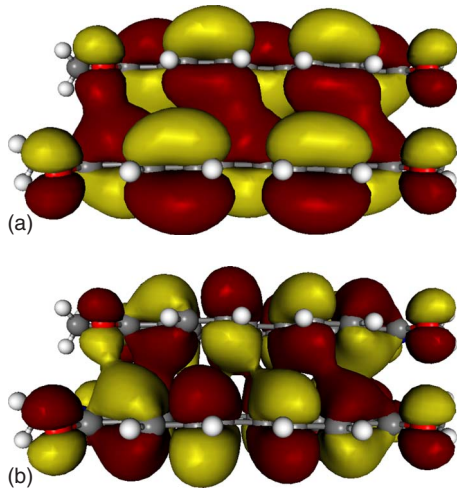
FIG. 4. (Color online) LUMO (upper) and HOMO (lower) of a stack of Me-PTCDI molecules in a geometry compatible with the crystalline phase calculated at the B3LYP/TZ level.

$$\psi_{\mathrm{LUMO}}^{\pm} = \frac{1}{\sqrt{2}} \begin{pmatrix} 1 \\ \pm 1 \end{pmatrix} \qquad (10)$$

and eigenvalues $E_{\mathrm{LUMO}}^{\pm} = E_{\mathrm{L}} \pm t_{\mathrm{L}}$. Therefore, the sign of the transfer parameter t_{L} can easily be obtained from visual inspection of the frontier orbitals in the dimer, compare Fig. 4 for Me-PTCDI: the LUMO turns out to be the state ψ_{LUMO}^{+} with the eigenvalue $E_{\mathrm{LUMO}}^{+} = E_{\mathrm{L}} + t_{\mathrm{L}}$, so that t_{L} has to be negative in order to have E_{LUMO}^{+} as the lower eigenvalue. Similarly, the HOMO in Fig. 4 is the state ψ_{HOMO}^{+} defined in analogy to Eq. (10), with the eigenvalue $E_{\mathrm{HOMO}}^{+} = E_{\mathrm{H}} + t_{\mathrm{H}}$ and positive t_{H}. From a second quantized Hamiltonian based on creation and annihilation of an electron in the HOMO or LUMO, it follows that the electron transfer is given by $t_e = t_{\mathrm{L}}$, but the hole transfer has the opposite sign with respect to the transfer between the HOMO orbitals on two adjacent stack neighbors, or $t_h = -t_{\mathrm{H}}$.

In the following, the signs of t_e and t_h as a function of the stacking geometry are analyzed with the B3LYP functional and a double-ζ (DZ) basis. The model geometries consist of two planar D_{2h}-symmetric PTCDI molecules optimized at the same B3LYP/DZ level, choosing a stacking distance of 3.4 Å along the molecular normal, in the same range as the values reported in Table VI. For this reference distance, the sign changes of the transfer parameters are determined by displacing the two molecules both along their long and short axes; compare Figs. 5 and 6.

For the electron transfer t_e, the sign can easily be related to the node pattern of the LUMO orbital in Fig. 2, but for the hole transfer, the situation is more complex. The node plane of the HOMO along the long axis of the molecule induces a sign change of t_h at a lateral displacement of about 2 Å, and the node planes of this orbital parallel to the short axis result in sign changes of t_h at longitudinal displacements around 1.3 and 3.9 Å. As the contour lines for vanishing t_h cannot cross, the node pattern is particularly complicated along equal longitudinal and transverse displacements around 2 Å.
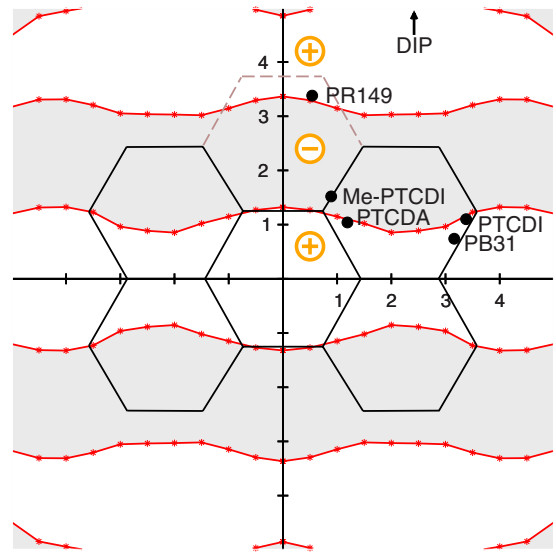
FIG. 5. (Color online) Calculated sign of the transfer parameter $t_{\mathrm{L}} = t_e$ between the LUMO states of two stacked PTCDI molecules at a distance of 3.4 Å along their normal: regions of positive transfer parameters (white), negative transfer parameters (gray), and contour lines of the sign changes (solid lines). The displacement along the long axis of the molecule is reported along the horizontal axis and the displacement along the short axis along the vertical. The dots indicate the projection of the stacking vector of five perylene compounds (α-PTCDA, Me-PTCDI, PB31, PTCDI, and PR149) with respect to the size of the perylene core of a free PTCDI molecule. The stacking geometry of DIP is outside of the range of displacements shown (arrow).

The sign of the transfer parameters in each pigment can be estimated from a stack of PTCDI molecules in a geometry resembling the arrangement in a specific crystal. In all pigments, the signs of the transfer parameters in Figs. 5 and 6 are well defined because the stacking geometries are never close to $t_h = 0$ or $t_e = 0$. The visualization of the stacking ge-
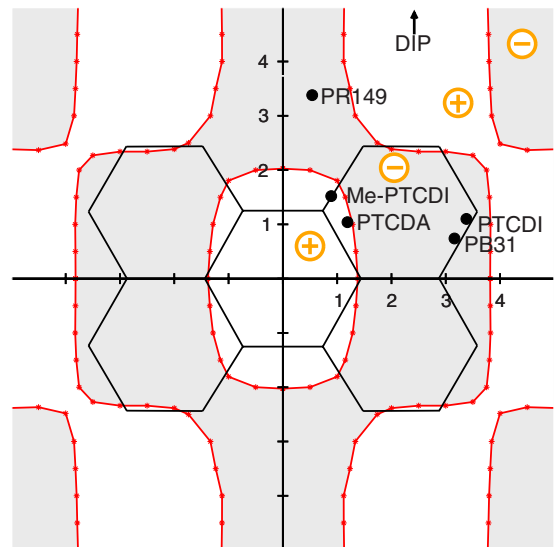
FIG. 6. (Color online) As in Fig. 5, but for the transfer $t_{\mathrm{H}} = -t_h$ between the HOMO states of two stacked PTCDI molecules.

TABLE VII. Comparison of calculated transfer parameters $t_h = -t_H$ and $t_e = t_L$, using Hartree-Fock or the hybrid functional B3LYP, in each case with two different variational basis sets for the electronic orbitals. For each compound, the calculations are based on a stacked dimer in a geometry compatible with the crystalline phase; compare Table VI. All entries are in eV.

Compound		HF/DZ	HF/TZ	B3LYP/DZ	B3LYP/TZ
α-PTCDA	t_h	−0.052	−0.054	−0.031	−0.034
	t_e	0.021	0.037	0.014	0.024
Me-PTCDI	t_h	−0.071	−0.073	−0.038	−0.041
	t_e	−0.160	−0.148	−0.111	−0.104
PB31	t_h	0.216	0.218	0.140	0.144
	t_e	0.117	0.128	0.078	0.083
PTCDI	t_h	0.150	0.151	0.098	0.102
	t_e	0.018	0.024	0.017	0.019
PR149	t_h	0.136	0.137	0.090	0.083
	t_e	0.035	0.030	0.022	0.020
DIP	t_h	−0.097	−0.099	−0.065	−0.066
	t_e	−0.042	−0.041	−0.034	−0.033

ometries in the various pigments indicates that the center of a molecule avoids a position above the center of a hexagon in the underlying molecule, a situation resembling graphite.

In order to keep track of the small influence of the side groups and the specific geometry of the perylene core in each compound, the values of the transfer parameters have to be recalculated for molecule pairs coinciding with the precise stacking geometry realized in the corresponding crystal.[2,46–50] Table VII compares the results of HF and B3LYP calculations, using in each case a double-ζ basis (DZ) and a triple-ζ (TZ) basis for the electronic states. The signs of the transfer parameters are independent of the computational approach and the variational basis set, but in several cases, the values obtained at the HF/TZ level are significantly larger than for the hybrid functional B3LYP/TZ. This indicates that the correlation included in the B3LYP functional produces more localized orbitals, so that the intermolecular transfer matrix elements are somewhat reduced. The results do not depend strongly on the variational basis set, so that we consider them to be reasonably well converged. Experimental information on the transfer parameters is restricted to the valence bandwidth $4|t_h|$ for two perylene compounds indicating a hole transfer of $|t_h| = 0.05$ eV for PTCDA and $|t_h| = 0.04$ eV for Me-PTCDI.[52,53] These experimental references do not allow to decide whether HF or DFT with the B3LYP functional is quantitatively more reliable: for PTCDA, HF seems to be slightly better, but the observed valence bandwidth of Me-PTCDI is clearly in favor of B3LYP. As interactions between the two basis molecules may contribute to the band dispersion, any comparison between observed bandwidth and a calculation restricted to the stack neighbors has to remain provisional.

Based on the transfer parameters reported in Table VII, in the exciton model discussed below we use values close to the results obtained at the B3LYP/TZ level. However, in selected cases, some deviations from these reference values seem to be unavoidable; compare Secs. VII and VIII for more details.

The electronic band structure arising from transfer along the stacking direction has the following dispersion:

$$E_{HOMO}(\mathbf{k}) = E_H + 2t_H \cos \mathbf{k} \cdot \mathbf{a}, \quad (11)$$

$$E_{LUMO}(\mathbf{k}) = E_L + 2t_L \cos \mathbf{k} \cdot \mathbf{a}, \quad (12)$$

$$E_{gap}(\mathbf{k}) = E_L - E_H + 2(t_L - t_H)\cos \mathbf{k} \cdot \mathbf{a}. \quad (13)$$

For the six model compounds, Fig. 7 visualizes the resulting valence band $E_{HOMO}(\mathbf{k})$ and the conduction band $E_{LUMO}(\mathbf{k})$ over the first Brillouin zone. The energies E_H and E_L are defined as the average energies of the pairs of frontier orbitals in a stack with a geometry compatible to the crystalline phase and the transfer parameters correspond to half of their splitting calculated with B3LYP/TZ; compare Table VII. PTCDA is the only material where the two transfer parameters t_H and t_L have the same sign, so that the gap between valence and conduction band has a particularly small dispersion.

In a single particle picture, optical excitations correspond to vertical transitions between valence and conduction band with the following first and second moments:

$$\langle E_{gap} \rangle = E_L - E_H, \quad (14)$$
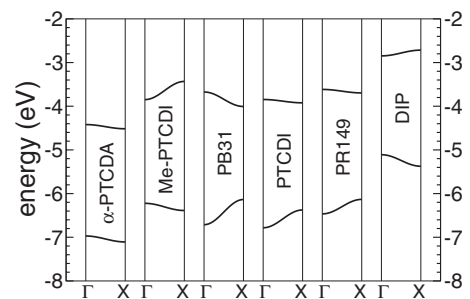
FIG. 7. Electronic band structure of the six model compounds based on B3LYP/TZ calculations for a stacked dimer in a geometry compatible with the respective crystalline phase.

TABLE VIII. Transition energies in a stack of two PTCDA molecules, obtained with CIS, TD-HF, and TD-DFT based on the B3LYP hybrid functional, using a TZ variational basis.

Compound	Dipole-allowed				Forbidden	
	E	f_{osc}	E	f_{osc}	E	E
	eV	1	eV	1	eV	eV
CIS	3.586	2.013	4.211	0.040	3.201	4.217
TD-HF	3.270	1.489	4.166	0.036	2.954	4.190
TD-DFT	2.116	0.015	2.618	0.956	2.078	2.328

$$\langle (\Delta E_{gap})^2 \rangle = 2(t_L - t_H)^2. \qquad (15)$$

In Sec. VI A, we shall discuss sum rules arising from our exciton model and compare them with Eqs. (14) and (15).

D. Transition dipoles of CT states

In a pair of stacked molecules, the frontier orbitals are linear superpositions of the respective states of a monomer, compare Eq. (10), with splittings given by twice the transfer parameters tabulated in Table VII. In the monoclinic space group of the pigments, the site symmetry of each molecule still contains the inversion and so does the point group of a stacked dimer. Therefore, instead of describing the transition energies in a dimer by a Hamiltonian based on the states of the monomers,

$$H = \begin{pmatrix} E_F & W & t_e & t_h \\ W & E_F & t_h & t_e \\ t_e & t_h & E_{CT} & V \\ t_h & t_e & V & E_{CT} \end{pmatrix}, \qquad (16)$$

it is suitable to decouple this Hamiltonian into subblocks of opposite parity, with

$$H^{(P=-1)} = \begin{pmatrix} E_F + W & t_e + t_h \\ t_e + t_h & E_{CT} + V \end{pmatrix} \qquad (17)$$

for the dipole-allowed and

$$H^{(P=+1)} = \begin{pmatrix} E_F - W & t_e - t_h \\ t_e - t_h & E_{CT} - V \end{pmatrix} \qquad (18)$$

for the dipole-forbidden transitions. Besides the fermionic transfer parameters t_e and t_h, the above Hamiltonian allows for the transfer of a neutral molecular excitation via the matrix element W between the transition charge densities of the neutral excitations on each site, and for the transfer between the two CT states via the matrix element V.

For a pair of stacked molecules, the transition energies and the transition dipoles can be obtained from different computational schemes including configuration interaction of singles (CIS), time-dependent Hartree-Fock (TD-HF), or TD-DFT, as reported in Table VIII for α-PTCDA. The two Hartree-Fock-based schemes place the CT states well above the neutral excitation with the large oscillator strength, whereas TD-DFT with the B3LYP hybrid functional results in a CT transition below the neutral excitation. From the

exciton model discussed in Secs. IV, VII, and VIII, in all six model compounds we find the CT states within a range of about ± 0.25 eV around the neutral excitations. From the large differences between the *ab initio* schemes applied to the computation of the transition energies, it is clear that all three attempts to compare a calculation for a pair of molecules to the crystalline phase have their weaknesses resulting both from the incomplete geometric model and from known systematic deficiencies of the methods used.

Inside the crystal, the polarization of the surroundings induces a redshift of CT transitions by about 2 eV with respect to an isolated dimer.[54–56] Moreover, the neutral molecular excitations in the crystal are redshifted by nearly 0.5 eV with respect to a monomer in weakly interacting surroundings[57] and with TD-DFT it can be investigated how different neighbors contribute to this effect.[28] For any microscopic investigation of a stacked dimer, the resulting transition energies will necessarily suffer from large energetic offsets with respect to a more complete description of the crystalline phase, so that approaches such as CIS, TD-HF, and TD-DFT can only generate raw data which will require further interpretation.

For TD-DFT, it is well known that the wrong asymptotics of the exchange-correlation functional is responsible for a distance dependence of the CT energy deviating from the $-1/r$ behavior expected from the Coulomb interaction.[58] However, from Table VIII, it is clear that this systematic deficiency of TD-DFT together with the missing polarizable surroundings brings the weakly absorbing CT states rather close to the strongly absorbing neutral excitation, resembling the situation in the crystal discussed in Secs. VII and VIII. Due to this compensation of errors, TD-DFT calculations of an isolated dimer become a quantitatively meaningful approach for an investigation of basic features of neutral excitations and CT states in the crystalline phase. Moreover, they have the advantage that the transitions of interest are well approximated by the HOMO-LUMO-based Hamiltonian (16), whereas in the HF-based schemes, one of the lowest dipole-allowed transitions has more than 10% admixture of transitions arising from other pairs of molecular orbitals.

In Table IX, we report the transition energies in stacked dimers of different perylene compounds obtained with TD-DFT at the B3LYP/TZ level. Among the two transitions of each parity, the lower is always dominated by CT transitions and the higher by neutral molecular excitations in keeping with the large difference between the respective oscillator strengths of the dipole-allowed transitions. Together with the

TABLE IX. Vertical transition energies in a stack of two molecules, in a geometry compatible with the monoclinic crystal phase, obtained with TD-DFT at the B3LYP/TZ level, except for PR149, which has been calculated with B3LYP/DZ.

Compound	Dipole-allowed				Forbidden	
	E	f_{osc}	E	f_{osc}	E	E
	eV	1	eV	1	eV	eV
α-PTCDA	2.116	0.015	2.618	0.956	2.078	2.328
Me-PTCDI	2.064	0.067	2.622	1.021	2.057	2.326
PB31	1.957	0.221	2.564	1.195	2.004	2.286
PTCDI	2.101	0.098	2.598	1.066	2.083	2.382
PR149	2.127	0.062	2.586	0.852	2.125	2.363
DIP	2.150	0.116	2.469	1.141	2.714	2.328

projection of the transitions onto pairs of Kohn-Sham orbitals, the TD-DFT results allow for the determination of the matrix elements W and V in Eqs. (16)–(18) and for an assignment of the transition dipoles between the localized frontier orbitals of the two molecules, compare Table X and the visualization for Me-PTCDI in Fig. 8. These values are calculated from the lowest two dipole-allowed transitions as obtained with TD-DFT under the assumption that the HOMO-LUMO transitions define the entire transition dipoles, without any contribution from the small contamination with transitions between other pairs of Kohn-Sham orbitals. Control calculations based on Hamiltonian (17) reveal that the size and direction of the transition dipole of the neutral molecular excitation is not sensitive to the incompleteness of this Hamiltonian with respect to the numerical TD-DFT results, but the small CT transition dipoles are more strongly affected. Irrespective of the type of analysis, the ratio μ_{CT}^2/μ_F^2 of the dipolar coupling strengths never exceeds 0.02.

In all compounds except for PTCDA, both dipole-allowed transitions in Table IX derive the main part of their oscillator strength from the large transition dipoles of the neutral molecular excitations. Thus, in general the weaker among the two dipole-allowed transitions is not a suitable measure for the transition dipole of the CT states. For Me-PTCDI, the four coplanar transition dipoles in Fig. 8 reveal the specific

linear superpositions of μ_F and μ_{CT} realized in the dimer transitions in Table IX. The orientation of the transition dipoles follows intuitive expectations: for the strong molecular transitions, they are aligned with the long axis of the molecule, just like the molecular HOMO-LUMO transition dipole, whereas the transition dipole of the CT state has an orientation rather close to the stacking direction.

In DIP, the transition dipole of the CT state is very small, and as opposed to the other compounds, it forms a rather large angle with the stacking direction, two features arising from the small geometric overlap between the molecules in the stack. Residual deviations from the ideal orientation of the transition dipoles for neutral excitation can be related to the incomplete covering of the lowest transitions found in TD-DFT by the four states underlying Eqs. (16)–(18): on average, for the molecules included in Table X, about 3% of the higher dipole-allowed transition arise from other pairs of Kohn-Sham orbitals modifying the direction of the resulting transition dipole by a small angle. In PR149 dimers, the specific orientation of the functional groups mixes transitions based on HOMO and LUMO of the monomers with transitions involving HOMO-1 and HOMO-2 states, so that an assignment of the transition dipoles from the B3LYP/TZ TD-DFT calculations would require a larger model Hamiltonian than Eq. (16). As this problem is less disturbing in a smaller

TABLE X. Vertical transition energies and transition dipoles of neutral molecular excitations and CT states in a stacked dimer determined from the values in Table IX, together with the orientation of the transition dipoles, expressed in terms of the angle α_{long} formed with the long axis of the molecules and the angle α_{stack} with respect to the stacking direction.

Compound	Neutral excitation			CT state		
	E_F (eV)	μ_F (D)	α_{long} (deg)	E_{CT} (eV)	μ_{CT} (D)	α_{stack} (deg)
α-PTCDA	2.470	6.93	1.8	2.101	0.94	15.0
Me-PTCDI	2.429	7.42	1.6	2.106	0.68	18.4
PB31	2.440	8.62	1.1	1.965	1.06	5.2
PTCDI	2.453	7.69	3.0	2.129	1.05	13.6
PR149	2.452	6.76	0.6	2.149	0.37	15.5
DIP	2.390	8.20	2.0	2.171	0.03	63.9
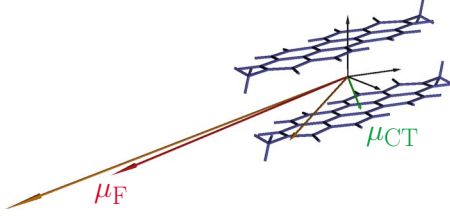
FIG. 8. (Color online) Transition dipoles in a stacked dimer of Me-PTCDI. Red: transition dipole μ_F of neutral molecular excitation; green: transition dipole μ_{CT} of CT transition; brown: transition dipoles calculated with TD-DFT.

DZ variational basis, we have analyzed this specific compound with TD-DFT calculations at the B3LYP/DZ level.

In the exciton model developed in the following, the ratio of the transition dipoles μ_{CT}/μ_F will be taken from the values in Table X. Concerning the direction of these dipoles, we shall assume that the neutral excitation has a transition dipole oriented exactly along the long axis of the molecule, whereas the CT states are handled with an orientation of their transition dipoles deduced from TD-DFT. As will be explained in Secs. VII and VIII in more detail, absolute values of the transition dipoles in the exciton model will be determined from a comparison to spectroscopic observations.

IV. EXCITON MODEL

A. Model Hamiltonian

For the perylene compounds studied in the present work, there is clear evidence that interactions between stack neighbors are dominating. Moreover, in all cases the HOMO-LUMO transition is rather strong and well separated from a weak transition at about 3.2 eV, so that is seems reasonable to restrict the exciton model to neutral excitations and CT states involving only the frontier orbitals. The fermionic transfer parameters t_e and t_h allow for a mixing between neutral molecular excitations and CT states on the same stack as visualized in Fig. 9.

In addition, the interaction between the dipolar transition densities of neutral excitations on different molecules can
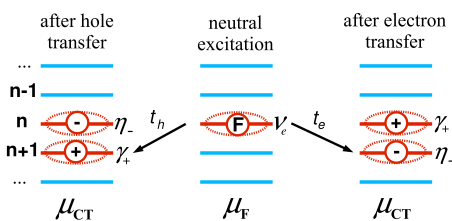
FIG. 9. (Color online) Visualization of three types of localized excited states in a one-dimensional stack of molecules. Center: neutral molecular excitation; left: CT state obtained from the neutral excitation after transferring a hole onto the neighboring site; right: CT state after transferring an electron. Each state can be obtained directly from the electronic ground state by an optical excitation governed by the large transition dipole μ_F of a molecular HOMO-LUMO transition or by the small intermolecular CT transition dipole μ_{CT}; compare Table X.

transfer these neutral excitations between the respective sites,[15] a mechanism investigated previously for the excitonic band structure of PTCDA and Me-PTCDI.[18–21] The TD-DFT studies of molecule pairs described in Sec. III D have demonstrated that the transfer parameter V between the two CT states on the same pair of molecules is much smaller than the transfer of a neutral excitation, so that it will be neglected in the following.

For different types of molecular crystals, including especially polyacenes, the fermionic transfers between the two basis molecules may be particularly large.[59] In these cases, the exciton model developed in the following should be extended to CT states involving both basis molecules, but for the compounds studied in the present work, we do not expect a significant influence of similar phenomena.

The model Hamiltonian can be divided into three parts: Frenkel (F) excitons based on neutral molecular excitations, CT states, and the interactions between them,

$$H^{tot} = H^F + H^{CT} + H^{F-CT}. \qquad (19)$$

Each molecule can occur in its electronic ground state, in an excited electronic state, and in positively or negatively charged ionized states. The electronic ground state shall be described as the lowest level of an effective internal vibration, so that the Born-Oppenheimer approximation results in a factorized wave function,

$$|g\rangle = \prod_{\mathbf{n}\alpha} |\phi^g_{\mathbf{n}\alpha} \chi^{0_g}_{\mathbf{n}\alpha}\rangle, \qquad (20)$$

with a ground-state electron configuration $|\phi^g_{\mathbf{n}\alpha}\rangle$ and a wave function $|\chi^{0_g}_{\mathbf{n}\alpha}\rangle$ corresponding to the lowest vibrational level on the basis molecule α in unit cell $\mathbf{n}$. The states visualized in Fig. 9 can be obtained by defining suitable excitation operators acting on the electronic ground state. An excitation toward the vibronic level ν_e of a neutral excited molecule shall be described by a creation operator $b^\dagger_{\mathbf{n}\alpha\nu_e}$,

$$b^\dagger_{\mathbf{n}\alpha\nu_e}|\phi^g_{\mathbf{n}\alpha}\chi^{0_g}_{\mathbf{n}\alpha}\rangle = |\phi^e_{\mathbf{n}\alpha}\chi^{\nu_e}_{\mathbf{n}\alpha}\rangle, \qquad (21)$$

where $|\phi^e_{\mathbf{n}\alpha}\rangle$ denotes the excited electronic configuration and $|\chi^{\nu_e}_{\mathbf{n}\alpha}\rangle$ the vibronic level ν_e in the excited potential; compare the stack visualized in the middle of Fig. 9. The creation of a CT state involves two neighboring molecules,

$$c^\dagger_{\mathbf{n}\alpha\eta_-;\mathbf{n}+1,\alpha\gamma_+}|\phi^g_{\mathbf{n}\alpha}\chi^{0_g}_{\mathbf{n}\alpha}\rangle|\phi^g_{\mathbf{n}+1,\alpha}\chi^{0_g}_{\mathbf{n}+1,\alpha}\rangle = |\phi^-_{\mathbf{n}\alpha}\chi^{\eta_-}_{\mathbf{n}\alpha}\rangle|\phi^+_{\mathbf{n}+1,\alpha}\chi^{\gamma_+}_{\mathbf{n}+1,\alpha}\rangle, \qquad (22)$$

with an anionic electronic configuration $|\phi^-_{\mathbf{n}\alpha}\rangle$ and a cationic state $|\phi^+_{\mathbf{n}+1,\alpha}\rangle$ on the neighboring site $\mathbf{R_n}+\mathbf{a}$, together with the vibronic levels η_- and γ_+ on the respective molecules; compare the left-hand side of Fig. 9. In this notation for the CT excitation, we use the convention that the basis molecule α in unit cell $\mathbf{n}$ shall carry an excess electron transferred from the neighboring molecule at the lattice vector $\mathbf{R_n}+\mathbf{a}$ which is losing an electron. Similarly, a charge separation in the opposite direction can be described as

$$c^{\dagger}_{\mathbf{n}\alpha\eta_-;\mathbf{n}-1,\alpha\gamma_+}|\phi^g_{\mathbf{n}\alpha}\chi^{0_g}_{\mathbf{n}\alpha}\rangle|\phi^g_{\mathbf{n}-1,\alpha}\chi^{0_g}_{\mathbf{n}-1,\alpha}\rangle = |\phi^-_{\mathbf{n},\alpha}\chi^{\eta_-}_{\mathbf{n},\alpha}\rangle|\phi^+_{\mathbf{n}-1,\alpha}\chi^{\gamma_+}_{\mathbf{n}-1,\alpha}\rangle \tag{23}$$

corresponding to the right-hand side of Fig. 9, shifted by one lattice vector. The excitations described by the creation operators in Eqs. (21)–(23) are the only states with a transition dipole toward the electronic ground state, whereas states involving vibronic excitations at sites differing from the molecules with modified electronic configurations cannot be excited from the electronic ground state, so that they will be ignored in the following. Depending on the Huang-Rhys factor of the effective mode, these states without dipolar coupling produce an additional energetic spreading of the transitions with dipolar coupling,[19] a phenomenon we shall include phenomenologically as an increased Gaussian broadening of higher vibronic levels.

The pure Frenkel part of the Hamiltonian in Eq. (19) describes neutral excitations of molecules and their transfer between different crystal sites,

$$H^{\mathrm{F}} = \sum_{\mathbf{n}\alpha\nu_e} E^{\mathrm{F}}_{0_g\nu_e} b^{\dagger}_{\mathbf{n}\alpha\nu_e} b_{\mathbf{n}\alpha\nu_e} + \sum_{\mathbf{n}\alpha\nu_e} \sum_{\mathbf{m}\beta\mu_e} t_{\mathbf{n}\alpha\nu_e;\mathbf{m}\beta\mu_e} b^{\dagger}_{\mathbf{n}\alpha\nu_e} b_{\mathbf{m}\beta\mu_e}, \tag{24}$$

where $E^{\mathrm{F}}_{0_g\nu_e} = E^{\mathrm{F}}_{0_g0_e} + \nu_e\hbar\omega$ is the molecular transition energy between the electronic and vibrational ground state and the vibronic level ν_e in the excited potential, using an effective internal vibration with energy $\hbar\omega$ in accordance to the DFT values in Table III. In this notation, the gas-to-crystal shift shall be included by a suitable choice of the lowest molecular transition energy $E^{\mathrm{F}}_{0_g0_e}$.

The matrix element $t_{\mathbf{n}\alpha\nu_e;\mathbf{m}\beta\mu_e}$ represents the transfer of an excitation from molecule α in unit cell $\mathbf{n}$ at vibronic level ν_e toward molecule β in unit cell $\mathbf{m}$ at vibronic level μ_e. This matrix element can be expressed as an electronic part arising from the interaction between the dipolar transition densities on both sites and vibronic Franck-Condon factors,

$$t_{\mathbf{n}\alpha\nu_e;\mathbf{m}\beta\mu_e} = \langle g b_{\mathbf{n}\alpha\nu_e}|H^{\mathrm{F}}|b^{\dagger}_{\mathbf{m}\beta\nu_e} g\rangle \tag{25}$$

$$= T_{\mathbf{n}\alpha;\mathbf{m}\beta} S_{0_g\nu_e} S_{0_g\mu_e}. \tag{26}$$

The Franck-Condon factors are defined via the Poisson progression over the transition probabilities,

$$S^2_{0_g\nu_e} = |\langle\chi^{0_g}|\chi^{\nu_e}\rangle|^2 = e^{-S}\frac{S^{\nu_e}}{\nu_e!}, \tag{27}$$

with the effective Huang-Rhys factor S for a neutral excited molecule from Table III. The electronic part $T_{\mathbf{n}\alpha;\mathbf{m}\beta}$ of the transfer of a neutral excitation will be discussed in Sec. IV B.

The second term in Eq. (19) represents the CT part of the Hamiltonian,

$$H^{\mathrm{CT}} = \sum_{\mathbf{m}\alpha} \sum_{\eta_-\gamma_+} E^{\mathrm{CT}}_{\eta_-\gamma_+}(c^{\dagger}_{\mathbf{n}\alpha\eta_-;\mathbf{n}+1,\alpha\gamma_+} c_{\mathbf{n}\alpha\eta_-;\mathbf{n}+1,\alpha\gamma_+}$$
$$+ c^{\dagger}_{\mathbf{n}\alpha\eta_-;\mathbf{n}-1,\alpha\gamma_+} c_{\mathbf{n}\alpha\eta_-;\mathbf{n}-1,\alpha\gamma_+}), \tag{28}$$

where $E^{\mathrm{CT}}_{\eta_-\gamma_+} = E^{\mathrm{CT}}_{00} + (\eta_- + \gamma_+)\hbar\omega$ denotes the energy of a CT state in the vibronic levels η_- and γ_+ of the anionic and the cationic site, respectively, and E^{CT}_{00} its lowest vibronic level. The last term in Eq. (19) allows for a mixing between neutral molecular excitations and CT states via electron and hole transfer,

$$H^{\mathrm{F-CT}} = \sum_{\mathbf{n}\alpha\nu_e} \sum_{\eta_-\gamma_+} [t'_h c^{\dagger}_{\mathbf{n}\alpha\eta_-;\mathbf{n}-1,\alpha\gamma_+} b_{\mathbf{n}\alpha\nu_e} + t'_h c^{\dagger}_{\mathbf{n}\alpha\eta_-;\mathbf{n}+1,\alpha\gamma_+} b_{\mathbf{n}\alpha\nu_e}$$
$$+ t'_e c^{\dagger}_{\mathbf{n}-1,\alpha\eta_-;\mathbf{n}\alpha\gamma_+} b_{\mathbf{n}\alpha\nu_e} + t'_e c^{\dagger}_{\mathbf{n}+1,\alpha\eta_-;\mathbf{n}\alpha\gamma_+} b_{\mathbf{n}\alpha\nu_e}] + \mathrm{H.c.}, \tag{29}$$

where t'_h and t'_e are abbreviations for hole and electron transfer, weighted with vibronic overlap factors,

$$t'_h = t_h S_{\nu_e\eta_-} S_{0_g\gamma_+}, \tag{30}$$

$$t'_e = t_e S_{\nu_e\gamma_+} S_{0_g\eta_-}, \tag{31}$$

with $S_{\nu_e\eta_-} = \langle\chi^{\nu_e}|\chi^{\eta_-}\rangle$, $S_{0_g\gamma_+} = \langle\chi^{0_g}|\chi^{\gamma_+}\rangle$, etc.

As the Frenkel part $\hat{H}^{\mathrm{F}}$ of the model Hamiltonian is restricted to vibronic states having a transition dipole toward the electronic and vibrational ground state, vibronic overlap factors between an excited vibrational level $|\chi^{\mu_g}\rangle$ in the electronic ground state and a vibronic level $|\chi^{\nu_e}\rangle$ in the excited state do not occur. Nevertheless, in the interaction part $H^{\mathrm{F-CT}}$ of the Hamiltonian, overlap factors of this kind are required because electron or hole transfer couples all vibronic levels of an excited molecule to the ones of the same molecule in its ionized state. Within the framework of the same effective internal vibration for the charged states and the excited state of a molecule, the inequality $S_+ < S_- < S$ discussed in Sec. II D allows the definition of positive Huang-Rhys factors for the deformation from an ionized state toward the optically excited state as

$$\widetilde{S}_+ = (\sqrt{S} - \sqrt{S_+})^2, \tag{32}$$

$$\widetilde{S}_- = (\sqrt{S} - \sqrt{S_-})^2. \tag{33}$$

With these Huang-Rhys factors, the vibronic overlap factors can be expressed as

$$S_{\nu_e\eta_-} = \langle\chi^{\nu_e}|\chi^{\eta_-}\rangle$$
$$= \frac{e^{-\widetilde{S}_-/2}}{\sqrt{\nu_e!\,\eta_-!}} \sum_{j=0}^{\min(\nu_e,\eta_-)} \frac{(-1)^{\nu_e-j}\widetilde{S}_-^{(\nu_e+\eta_--2j)/2}\nu_e!\,\eta_-!}{j!\,(\nu_e-j)!\,(\eta_--j)!}, \tag{34}$$

and the overlap factors $S_{\nu_e\gamma_+}$ relating cation and excited state can be calculated similarly.

B. Block diagonalization by Fourier transform

In a periodic system, we can perform a Fourier transformation of all operators into wave vector representation[60] allowing for a block diagonalization of the model Hamiltonian. From the operators $b^{\dagger}_{\mathbf{n}\alpha\nu_e}$ describing a neutral excitation of a specific molecule, we go over to the excitation of a Bloch wave with wave vector $\mathbf{k}$ defined as a superposition of neutral excitations at specific sites,

$$b_{\mathbf{k}\alpha\nu_e}^\dagger = \frac{1}{\sqrt{N}}\sum_{\mathbf{n}} e^{-i\mathbf{k}\cdot\mathbf{R}_{\mathbf{n}\alpha}} b_{\mathbf{n}\alpha\nu_e;\mathbf{n}0_g}^\dagger, \tag{35}$$

where $\mathbf{R}_{\mathbf{n}\alpha}=\mathbf{R}_{\mathbf{n}}+\mathbf{r}_\alpha$ is the position of the basis molecule α in the crystal unit cell $\mathbf{n}$. In analogy to this expression for the creation of a Frenkel exciton with wave vector $\mathbf{k}$, we transform the CT excitations into their wave vector representation,

$$c_{\mathbf{k}\alpha\eta_-\gamma_+,+}^\dagger = \frac{1}{\sqrt{N}}\sum_{n} e^{-i\mathbf{k}\cdot\mathbf{R}_{\mathbf{n}\alpha}} c_{\mathbf{n}\alpha\eta_-;\mathbf{n}+1,\alpha\gamma_+}^\dagger, \tag{36}$$

$$c_{\mathbf{k}\alpha\eta_-\gamma_+,-}^\dagger = \frac{1}{\sqrt{N}}\sum_{n} e^{-i\mathbf{k}\cdot\mathbf{R}_{\mathbf{n}\alpha}} c_{\mathbf{n}\alpha\eta_-;\mathbf{n}-1,\alpha\gamma_+}^\dagger, \tag{37}$$

where the last index $+$ or $-$ addresses the relative position of the cationic molecule with respect to the anionic site, so that the operator $c_{\mathbf{k}\alpha\eta_-\gamma_+,+}^\dagger$ describes Bloch waves of the CT states visualized on the left-hand side of Fig. 9, and accordingly, the operator $c_{\mathbf{k}\alpha\eta_-\gamma_+,-}^\dagger$ corresponds to its right-hand side. The creation operators relating to specific sites can be expressed by the inverse of these discrete Fourier transforms. Inserting them into the model Hamiltonian, blocks for different wave vectors $\mathbf{k}$ decouple:

$$H^{\text{tot}}(\mathbf{k}) = \sum_{\mathbf{k}} H^{\text{F}}(\mathbf{k}) + H^{\text{CT}}(\mathbf{k}) + H^{\text{F–CT}}(\mathbf{k}). \tag{38}$$

With respect to the two basis molecules A and B, this Hamiltonian has the following block structure:

$$H^{\text{tot}}(\mathbf{k}) = \begin{pmatrix} H_{AA}^{\text{F}}(\mathbf{k}) & H_{AA}^{\text{F–CT}}(\mathbf{k}) & H_{AB}^{\text{F}}(\mathbf{k}) & 0 \\ \text{H.c.} & H_{AA}^{\text{CT}}(\mathbf{k}) & 0 & 0 \\ \text{H.c.} & \text{H.c.} & H_{BB}^{\text{F}}(\mathbf{k}) & H_{BB}^{\text{F–CT}}(\mathbf{k}) \\ \text{H.c.} & \text{H.c.} & \text{H.c.} & H_{BB}^{\text{CT}}(\mathbf{k}) \end{pmatrix}, \tag{39}$$

highlighting that the only mechanism coupling the basis molecules results from the transfer of neutral excitations, whereas CT states involving both basis molecules are neglected and a CT Bloch wave localized on molecules A does not couple to the respective Bloch wave involving only basis molecules B. The subblocks for the Frenkel excitons read

$$H_{\alpha\beta}^{\text{F}}(\mathbf{k}) = \delta_{\alpha\beta}\sum_{\nu_e} E_{0_g\nu_e}^{\text{F}} b_{\mathbf{k}\alpha\nu_e}^\dagger b_{\mathbf{k}\beta\nu_e}$$
$$+ \sum_{\nu_e,\mu_e} S_{0_g\nu_e} S_{0_g\mu_e} T_{\alpha\beta}(\mathbf{k}) b_{\mathbf{k}\alpha\nu_e}^\dagger b_{\mathbf{k}\beta\mu_e}, \tag{40}$$

where

$$T_{\alpha\beta}(\mathbf{k}) = \sum_{\mathbf{R}_{\mathbf{n}\alpha;\mathbf{m}\beta}\neq 0} e^{-i\mathbf{k}\cdot\mathbf{R}_{\mathbf{n}\alpha;\mathbf{m}\beta}} T_{\mathbf{n}\alpha;\mathbf{m}\beta} \tag{41}$$

is the Fourier transform of the excitation transfer and $\mathbf{R}_{\mathbf{n}\alpha;\mathbf{m}\beta}=\mathbf{R}_{\mathbf{n}\alpha}-\mathbf{R}_{\mathbf{m}\beta}$ the distance vector between two molecules. Since the monoclinic space group of the molecular crystals investigated has a center of inversion, the exciton transfer matrix elements $T_{\alpha\beta}(\mathbf{k})$ are real and symmetric with respect to the indices of the basis molecules A and B,[15] re-

sulting in $T_{AA}(\mathbf{k})=T_{BB}(\mathbf{k})$ and $T_{AB}(\mathbf{k})=T_{BA}(\mathbf{k})$.

As we have assumed that the transfer of a CT state can be neglected, the subblocks $H_{AA}^{\text{CT}}(\mathbf{k})=H_{BB}^{\text{CT}}(\mathbf{k})$ consist only of diagonal elements $E_{\gamma_+\eta_-}^{\text{CT}}$ for each vibronic level. The off-diagonal blocks mixing the vibronic levels ν_e of a Frenkel exciton and the vibronic levels η_- and γ_+ on the anionic and cationic site of a CT Bloch wave involve contributions from different localized excitations. Restricting the following discussion to states according to the left-hand side of Fig. 9, the relevant localized CT excitations mixing with a neutral excitation on site $\mathbf{n}$ are described by the operators $c_{\mathbf{n}\alpha\eta_-;\mathbf{n}+1,\alpha\gamma_+}^\dagger$ and $c_{\mathbf{n}-1\alpha\eta_-;\mathbf{n},\alpha\gamma_+}^\dagger$, where, in the first case, the previously neutrally excited site $\mathbf{n}\alpha$ is acquiring a negative charge, so that the hole is transferred, and in the second case, the molecule $\mathbf{n}\alpha$ loses an electron, which is transferred to basis molecule α in unit cell $\mathbf{n}-1$. As a result, the mixing of a Frenkel exciton with a Bloch wave of CT states contains an interference of electron and hole transfer, so that the mixing of neutral and charged excitation reads

$$H_{\alpha\alpha}^{\text{F–CT}}(\mathbf{k}) = \sum_{\nu\eta_-\gamma_+} [c_{\mathbf{k}\alpha\eta_-\gamma_+,-}^\dagger b_{\mathbf{k}\alpha\nu}(t_h' + e^{-i\mathbf{k}\cdot\mathbf{a}}t_e')$$
$$+ c_{\mathbf{k}\alpha\eta_-\gamma_+,+}^\dagger b_{\mathbf{k}\alpha\nu}(t_h' + e^{i\mathbf{k}\cdot\mathbf{a}}t_e')] \tag{42}$$

with the transfer matrix elements t_e' and t_h' containing the Franck-Condon factors according to Eqs. (30) and (31).

The Frenkel excitons on the A and B basis molecules are coupled by the off-diagonal element $H_{AB}^{\text{F}}(\mathbf{k})$ in Eq. (39), but a decoupling can be achieved by a superposition of both basis molecules governed by Hamiltonians

$$H_{AA}^{\text{F}}(\mathbf{k}) \pm H_{AB}^{\text{F}}(\mathbf{k}). \tag{43}$$

In terms of the creation operators of Frenkel excitons, this further block diagonalization can be expressed by a superposition of Bloch waves involving A or B basis molecules:

$$b_{\mathbf{k}\xi\nu_e}^\dagger = \frac{1}{\sqrt{2}}(b_{\mathbf{k}A\nu_e}^\dagger \pm b_{\mathbf{k}B\nu_e}^\dagger). \tag{44}$$

Accordingly, a similar procedure applied to the CT states reads

$$c_{\mathbf{k}\xi\eta_-\gamma_+\sigma}^\dagger = \frac{1}{\sqrt{2}}(c_{\mathbf{k}A\eta_-\gamma_+\sigma}^\dagger \pm c_{\mathbf{k}B\eta_-\gamma_+\sigma}^\dagger), \tag{45}$$

where $\xi=y$ governed by the upper sign represents Bloch waves with transition dipoles exclusively along y, coinciding with the screw axis in the monoclinic space group, and the difference indexed $\xi=x$ has molecular transition dipoles along x and CT transition dipoles in the xz plane. After expressing the Hamiltonian with these new operators, the two decoupled subblocks read

$$H_\xi^{\text{tot}}(\mathbf{k}) = \begin{pmatrix} H_{AA}^{\text{F}}(\mathbf{k}) \pm H_{AB}^{\text{F}}(\mathbf{k}) & H_{AA}^{\text{F–CT}}(\mathbf{k}) \\ \text{H.c.} & H_{AA}^{\text{CT}}(\mathbf{k}) \end{pmatrix}. \tag{46}$$

The vibronic levels included in the model Hamiltonian are restricted to the ones with contributions above 10^{-6} to the Poisson progressions obtained from the Huang-Rhys factors in Table III. Using the largest Huang-Rhys factors occurring,

this restricts the range of the vibronic levels required to 0–9 for neutral excitations, 0–8 for anionic states, and 0–6 for cationic states. The product space needed for each type of CT state contains therefore 63 vibronic levels including several with relative weight below the threshold of 10^{-6}. We did not attempt to eliminate the respective basis states, and the diagonalization of Hamiltonian (46) was performed numerically with LAPACK routines.

C. Optical properties

After diagonalization of the model Hamiltonian for vanishing wave vector $\mathbf{k}=0$, the elements of the dielectric tensor can be related to the respective transition dipoles. We denote the transition dipoles of the eigenstates as $\mathbf{d}_{0\xi j}$, where $\xi = y, x$ describes the two kinds of eigenstates contributing to ϵ_{yy} along the lattice vector $\mathbf{b}$ or to the elements of the dielectric tensor in the ac plane, respectively, and the last index j counts the eigenstates obtained. In the more general case of the ac plane, the 2×2 dielectric tensor can be obtained as

$$\underline{\underline{\epsilon}}(\omega) = 1 + \chi_b(\omega) + \frac{2}{\epsilon_0 V \hbar} \sum_j \mathbf{d}_{0xj} \mathbf{d}_{0xj}^t$$
$$\times \left[\frac{1}{\omega_{0xj} - \omega - i\Gamma} + \frac{1}{\omega_{0xj} + \omega + i\Gamma} \right], \quad (47)$$

where an infinitesimal damping Γ guarantees causality and the frequency-dependent background $\chi_b(\omega) = \chi_b(0)\Omega^2/(\Omega^2 - \omega^2)$ arises from transitions at $\hbar\Omega$ far above the HOMO-LUMO contribution calculated from our model Hamiltonian. The product between the column vector $\mathbf{d}_{0xj}$ and the row vector $\mathbf{d}_{0xj}^t$ generates the tensor structure of $\underline{\underline{\epsilon}}$. In the comparison with the experimental data in Sec. VIII, we shall only discuss the element $\epsilon_{xx}(\omega)$ dominated by neutral excitation of molecules, disregarding the small contributions to other tensor elements arising from the orientation of the CT transition dipole, but in principle, these tensor elements are contained in our calculations. The part of the CT transition dipole along x gives a small contribution to $\epsilon_{xx}(\omega)$ which will be included in the comparison with the measured data. The transition dipoles $\mathbf{d}_{0yj}$ are oriented along y so that a construction similar to Eq. (47) gives just the element ϵ_{yy} of the dielectric tensor.

Due to elongations of low-frequency internal vibrations and external phonons, the contribution of each eigenstate j to the dielectric tensor will be subject to a Gaussian broadening. These broadenings will be chosen according to the observed absorption coefficient or dielectric function, so that in Eq. (47) the contribution of each eigenstate j to the imaginary part will be replaced by a suitable normalized Gaussian and the real part will be obtained from a Kramers-Kronig transform.

V. DATA ANALYSIS

As information on both components of the dielectric tensor is only available in exceptional cases,[22,32,61] we start with the analysis of published information concerning optical density and reflectivity of thin films or single crystals before
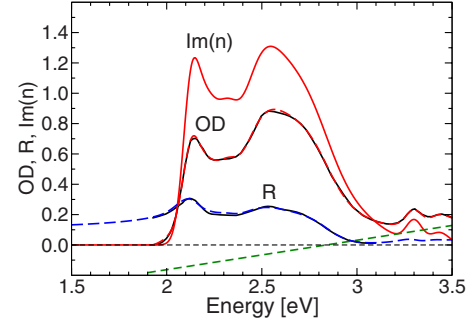
FIG. 10. (Color online) Optical density (OD), reflectivity (R), and extinction coefficient $\Im(n)$ of Me-PTCDI, at room temperature. Black: observed optical density of thin film with a thickness of about 100 nm and reflectivity of a single crystal with electric field polarized along the lattice vector $\mathbf{b}$ (Ref. 11); red dashed: fit to optical density; green dashed: assumed linear baseline underlying the published optical density; blue dashed: fit to reflectivity; red solid line: resulting extinction coefficient $\Im(n)$. The fits are relying on a Kramers-Kronig consistent model for the refractive index.

proceeding to the parametrization of the Frenkel-CT model. Optical density and reflectivity R provide complementary information on real and imaginary part of the refractive index. The optical density is defined as the logarithm of the transmission T,

$$\text{OD} = -\log_{10} T. \quad (48)$$

Ignoring interference effects, the transmission is given by

$$T = e^{-\alpha d}(1-R)^2, \quad (49)$$

where $\alpha = 2(\omega/c)\Im(n)$ is the absorption coefficient proportional to the extinction coefficient $\Im(n)$ and R is the reflectivity. When the organic film is grown on a substrate like glass, this formula can be generalized to different reflectivities of the front and rear surfaces of the film. In the following, such differences will be ignored. From the exponential in the definition of T, one expects the optical density to be proportional to the extinction coefficient, but the correction factor $(1-R)^2$ generates energy-dependent deviations. Moreover, published values for the optical density tend to suppress an energy-dependent slope in order to have a closer analogy to the extinction coefficient.

For the reference case of Me-PTCDI films studied at room temperature, digitized published data for the optical density and the reflectivity are presented in Fig. 10.[11] In the fitting procedure, we have defined a Kramers-Kronig consistent model function for the complex refractive index n and then we have optimized all parameters involved. The extinction coefficient $\Im(n)$ was modeled as a sum of Gaussians, and in order to facilitate an analytical Kramers-Kronig transform, each Gaussian was replaced by a suitable superposition of absorptive Lorentzians, with weights and relative widths kept at the same values with respect to a normalized Gaussian. Moreover, the model for the real part of the refractive index $\Re(n)$ accounts for a frequency-dependent background arising from a sharp transition at much higher energy, similar to the background contribution to $\Re(\epsilon)$ in Eq. (47), so that this background function does not generate a contribution to

$\Im(n)$ in the energetic range of interest. We found clear evidence that the published optical density was corrected for a frequency-dependent background, compare Fig. 10, and we assumed that this background was described by a linear dependence on energy. The area and broadening of the different subbands can easily be obtained from the optical density, but without additional information on the reflectivity, it would not be possible to determine reliable values for the background of $\Re(n)$. Therefore, we alternated between fits of the Gaussian subbands contributing to $\Im(n)$ and an adjustment of the background of $\Re(n)$. As a result of this fitting procedure, we have determined a Kramers-Kronig consistent model for the complex refractive index n, and as visualized in Fig. 10, optical density and reflectivity calculated from this model give excellent agreement with the observed data.

The optical density was measured on a polycrystalline film with random azimuthal orientation of the crystallites, so that about 90% of the absorption arises from the large diagonal component ϵ_{yy} of the dielectric tensor and 10% from the small component ϵ_{xx}; compare Table V. In the fit, we have assumed that both components have the same energy dependence. The modulation of the calculated reflectivity curve for a thick crystal depends on the film thickness assumed in the fit of the measured optical density, and we found the best agreement at the reflectivity extrema occurring at 2.12 and 3.10 eV for a fixed film thickness of 86 nm in the fit of the optical density, in reasonable agreement with the experimental estimate of about 100 nm. Our best value for the film thickness was based on visual inspection of the agreement between calculated and measured reflectivity curve, as opposed to a fit of a free thickness parameter. Therefore, we give a conservative estimate of $d = 86 \pm 5$ nm for the film thickness underlying our analysis excluding uncertainties of the absolute scale of the measured data which were not reported. Figure 10 demonstrates that the reflectivity corrections in the definition of the optical density are responsible for significant deviations between the shape of the observed optical density and the underlying extinction coefficient $\Im(n)$.

VI. APPROXIMATE PARAMETERS FOR FRENKEL EXCITONS

In the F-CT model described in Sec. IV, there are four groups of parameters: internal deformations treated with the effective mode energies and Huang-Rhys factors summarized in Table III, fermionic transfer parameters t_e and t_h mixing F and CT excitations, with numerical values as discussed in Sec. III C, transfer of neutral molecular excitations, and energies of neutral excitations and CT states. In this section, we shall provide starting values for the three parameters describing the Frenkel exciton manifold, i.e., the energy of the lowest molecular transition E_{00}^F, and the two transfer parameters $T_{AA}(\mathbf{k}=\mathbf{0})$ and $T_{AB}(\mathbf{k}=\mathbf{0})$, the latter governing the Davydov splitting between the vibronic subbands observed in the diagonal components ϵ_{xx} and ϵ_{yy} of the dielectric tensor. In the following, the large gas-to-crystal shift occurring in molecular crystals[9,57] shall be included in the chosen value of E_{00}^F. Therefore, due to different requirements of the mod-

els discussed in Secs. VI and VII, a suitable value of the lowest molecular transition E_{00}^F depends on the specific context.

A. Sum rules for exciton transfer

The Kramers-Kronig consistent model for the refractive index allows to calculate the underlying dielectric function as $\Re(\epsilon) = [\Re(n)]^2 - [\Im(n)]^2$ and $\Im(\epsilon) = 2\Re(n)\Im(n)$. In a pure Frenkel exciton model accounting only for the transfer of neutral molecular excitations between different sites, it can be shown that the average transition energy depends in a very simple way on the lowest molecular transition E_{00}^F, the internal reorganization energy $\lambda = S\hbar\omega$, and the transfer of excitons:[24–26]

$$\langle E \rangle = E_{00}^F + S\hbar\omega + T, \tag{50}$$

where $T = T_{AA}(\mathbf{0}) \pm T_{AB}(\mathbf{0})$ is the transfer matrix element for a specific component of the dielectric tensor and the energy average $\langle E \rangle$ is calculated from the line shape of $\Im(\epsilon)$. For pure CT states, the average transition energy corresponds to

$$\langle E \rangle = E_{00}^{CT} + (S_+ + S_-)\hbar\omega. \tag{51}$$

In a mixed Frenkel-CT model, the average transition energy has to account for the weight of each type of transition according to the respective transition dipoles discussed in Sec. III D, and the mixing of Frenkel and CT states via H^{F-CT} does not result in any modification. In a pure Frenkel model, it was shown previously that the second moment of the optical response does not depend on exciton transfer[26]

$$\langle (\Delta E)^2 \rangle = S(\hbar\omega)^2. \tag{52}$$

In the limit of vanishing transition dipole of the CT states, our mixed Frenkel-CT model gives a particularly simple formula for the increase in the second moment,

$$\langle (\Delta E)^2 \rangle = S(\hbar\omega)^2 + 2(t_e + t_h)^2, \tag{53}$$

where the contribution arising from electron and hole transfer reproduces the second moment obtained in a single particle picture; compare Eq. (15).

B. Line shape obtained from Frenkel excitons

As the results of the full model will be discussed in the next section, here we provide only Frenkel exciton parameters determined from a comparison of Eq. (50) with the average transition energy. The lowest transition contributing to the dielectric function corresponds to the lowest dispersion branch at the Γ point of the Brillouin zone, $E_{00}^F(\mathbf{0})$, not to the molecular parameter E_{00}^F occurring in the sum rule Eq. (50). Using a pure Frenkel exciton model, the difference between these two values can easily be obtained numerically.

In Fig. 11 we compare the dielectric tensor element $\Im(\epsilon_{yy})$ of Me-PTCDI with the result of a Frenkel exciton model based on parameters giving the same average transition energy $\langle E \rangle$ together with the observed value for the lowest subband which is assigned to $E_{00}^F(\mathbf{0})$. This procedure allows to determine an approximate exciton transfer $T = T_{AA}(\mathbf{0}) + T_{AB}(\mathbf{0})$ governing this element of the dielectric tensor. As
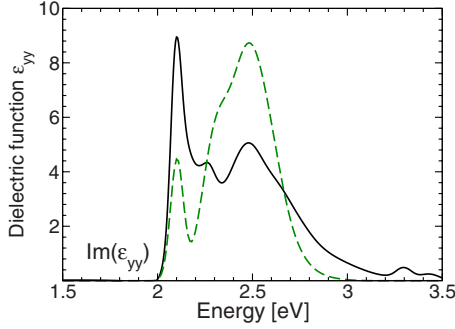
FIG. 11. (Color online) Imaginary part of the dielectric tensor element ϵ_{yy} derived from the measured optical density at $T=20$ K (Ref. 11) (black), and calculation based on a pure Frenkel exciton model (green dashed), with parameters chosen according to the sum rule in Eq. (50); compare Table XI.

the only evidence for the shape of the other diagonal element ϵ_{xx} is restricted to a reflectivity curve with similar shape as the one included in Fig. 10, but with reduced modulation, we assume that both tensor elements ϵ_{xx} and ϵ_{yy} coincide except for the size related to the respective dipolar coupling strength. This corresponds to a vanishing Davydov splitting or a vanishing exciton transfer $T_{AB}(\mathbf{0})=0$ between the two basis molecules.

The parameters derived for the pure Frenkel exciton model reproduce the observed values $\langle E \rangle$ and the position of the lowest subband $E_{00}^{\mathrm{F}}(\mathbf{0})$, compare Table XI, but as visualized in Fig. 11, the model is not flexible enough for obtaining a quantitative agreement with the observed intensities of the various subbands, so that the second moment remains far below the respective value deduced from the observed line shape. According to Eq. (53), the too narrow absorption band arising from the pure Frenkel exciton model reveals the need to account for the interference of Frenkel and CT transitions via electron and hole transfer. Notwithstanding the obvious deficiencies visualized in Fig. 11, the pure Frenkel exciton model can be used for the definition of suitable starting values for E_{00}^{F} and the matrix element governing the transfer of

neutral excitations. Moreover, for PTCDA, the anisotropy of the optical observables measured by spectroscopic ellipsometry allows to determine values of both $T_{AA}(\mathbf{0})$ and $T_{AB}(\mathbf{0})$.[22,61]

C. Temperature dependence of optical observables

Previous studies of the temperature dependence of the lattice vectors have revealed that the stacking vector of Me-PTCDI and PR149 shrinks by at least 1% when going from room temperature to low temperature.[11] At room temperature, the anisotropic thermal expansion coefficients are of the order of 1×10^{-4} K^{-1}, and for PTCDA, the expansion coefficient along the stacking vector even exceeds this value.[11,63] Assuming that the temperature dependence of the stacking vector in PTCDA remains particularly large when cooling the material, it can be estimated that its reduction should be around 1.5% when going to very low temperature. The calculated dependence of the CT transition energy on the stacking vector of 0.5 eV Å^{-1} (Ref. 28) gives an estimate of about 0.02–0.03 eV for the resulting redshift of the CT transition. Energetic shifts in this range are consistent with the pressure dependence and the temperature dependence of photoluminescence from CT states.[64,65] Concerning absorption spectra of PTCDA, a line shape analysis of low-temperature spectra reveals a redshift of the lowest Frenkel subband by about 0.02 eV with respect to ellipsometry or absorption obtained at room temperature[18,22,66,67] indicating that the temperature dependence of CT states and neutral excitations is similar.

For Me-PTCDI, the observed optical density at $T=20$ K contains sharper structures consistent with a redshift of the neutral molecular excitation by about 0.02 eV and a reduced broadening; compare Table XI. For simplicity, we assume that neutral molecular excitations and CT transitions shift in the same way as a function of temperature, or by -0.02 eV when reducing the temperature to $T=20$ K.

In the following, we shall analyze room-temperature optical data for most materials, but in addition, for Me-PTCDI,

TABLE XI. Model parameters for a pure Frenkel exciton model. The effective mode and its Huang-Rhys factor S are taken from Table III, and the exciton transfer parameters are determined according to the sum rule in Eq. (50) and the lowest observed subband, assigned to $E_{00}^{\mathrm{F}}(\mathbf{0})$ at Γ. The average observed excitation energy $\langle E \rangle$ of the HOMO-LUMO transition is obtained from an analysis of measured spectra, excluding the higher transition around 3.3 eV. The parameter $T_{AB}(\mathbf{0})$ responsible for Davydov splitting can only be addressed for PTCDA where a pronounced anisotropy of the dielectric tensor was observed (Refs. 22 and 61).

	T (K)	$\langle E \rangle$ (eV)	E_{00}^{F} (eV)	$S\hbar\omega$ (eV)	$T_{AA}(\mathbf{0})$ (eV)	$T_{AB}(\mathbf{0})$ (eV)	$E_{00}^{\mathrm{F}}(\mathbf{0})$ (eV)
PTCDA ϵ_{xx} (Ref. 61)	300	2.40	2.20	0.15	0.095	0.045	2.22
PTCDA ϵ_{yy} (Ref. 61)	300	2.49	2.20	0.15	0.095	0.045	2.25
Me-PTCDI (Ref. 11)	20	2.43	2.05	0.15	0.23		2.10
Me-PTCDI (Ref. 11)	300	2.46	2.08	0.15	0.23		2.13
PB31 (Ref. 11)	12	2.36	1.96	0.15	0.25		2.01
PTCDI (Ref. 62)	300	2.39	2.06	0.14	0.19		2.11
PR149 (Ref. 11)	20	2.51	2.14	0.15	0.22		2.19
DIP (Ref. 32)	300	2.48	2.22	0.15	0.11		2.25

TABLE XII. Parameters of the Frenkel-CT model, with $\Delta_{00}=E_{00}^{\mathrm{CT}}-E_{00}^{\mathrm{F}}$. In all cases, the electron and hole transfer parameters giving the best agreement with the observed data are close to the B3LYP/TZ values in Table VII, but systematically smaller than the HF/TZ values. The intramolecular deformation parameters are chosen according to Table III.

Compound	T (K)	E_{00}^{F} (eV)	E_{00}^{CT} (eV)	Δ_{00} (eV)	$T_{AA}(\mathbf{0})$ (eV)	$T_{AB}(\mathbf{0})$ (eV)	t_h (eV)	t_e (eV)	μ_{F} (D)
PTCDA ϵ_{xx}	300	2.17	1.95	-0.22	0.14	0.05	-0.034	0.024	7.02
PTCDA ϵ_{yy}	300	2.17	1.95	-0.22	0.14	0.05	-0.034	0.024	6.75
Me-PTCDI	20	2.18	2.24	0.06	0.08	0.00	-0.020	-0.090	5.98
Me-PTCDI	300	2.20	2.26	0.06	0.08	0.00	-0.020	-0.090	5.98
PB31	12	2.195	2.325	0.13	0.01	0.00	0.144	0.053	10.38
PTCDI	300	2.18	2.31	0.13	0.06	0.00	0.076	0.019	7.06
PR149	20	2.155	2.365	0.21	0.12	0.00	0.088	0.015	7.33
DIP	300	2.255	2.535	0.28	0.095	0.00	-0.056	-0.033	8.10

the availability of temperature-dependent observables will be addressed explicitly. For PB31 and PR149, observables at low temperature show somewhat sharper structures, so that they are better suited for an assignment of the parameters required in the exciton model. Therefore, for these specific materials, we shall restrict the discussion to low-temperature data.

VII. INTERFERENCE OF FRENKEL EXCITONS AND CT TRANSITIONS

In the previous section, a pure Frenkel exciton model with parameters chosen according to the sum rule in Eq. (50) was able to reproduce the energy of the lowest vibronic subband and the average transition energy $\langle E \rangle$, but from the poor agreement with the dielectric function of Me-PTCDI visualized in Fig. 11, it is obvious that the second moment of the calculated line shape is much too narrow. This indicates that the pure Frenkel model is ignoring a fundamental interaction mechanism leading to an additional spreading of the calculated dielectric function over a larger energetic range. In the following, it will be demonstrated that the Frenkel-CT interference via electron and hole transfer can account quantitatively for these features.

In the Frenkel-CT model, if the CT energy is above the molecular transition energy, the interaction between both types of excitations pushes the lowest vibronic subband of the Frenkel exciton down in energy. Therefore, the lowest molecular transition E_{00}^{F} has to be chosen at a higher energy with respect to Table XI. Accordingly, the exciton transfer $T_{AA}(\mathbf{0})$ has to be reduced in order to avoid a calculated average transition energy $\langle E \rangle$ exceeding the observed value. Both modifications of the model parameters will be more pronounced for materials with particularly large electron and hole transfer. PTCDA differs from this behavior in two respects: first, E_{00}^{CT} is placed below E_{00}^{F}, and second, the parameters for electron and hole transfer are particularly small, so that the preliminary parameters in Table XI are expected to remain rather reliable. As the energetic ordering of the two basic types of excitations differs from the other materials, the Frenkel-CT interference will push the lowest subband of the Frenkel exciton upward so that the respective model param-

eter E_{00}^{F} has to be chosen at a value slightly below the respective entry of Table XI.

From the discussion in Sec. III D, it became clear that TD-DFT applied to pairs of molecules does not allow deducing realistic energies for the CT transitions. Hence, the lowest CT subband E_{00}^{CT} will be treated as a free fitting parameter and the inclusion of Frenkel-CT mixing with electron and hole transfer matrix elements resembling the entries in Table VII will induce systematic shifts of the parameters describing the Frenkel part of the model with respect to the values in Table XI.

The final model parameters for the six perylene compounds are summarized in Table XII. For all materials, electron and hole transfer parameters close to the B3LYP/TZ values in Table VII yield an excellent agreement with observed line shapes of the refractive index or dielectric tensor. The detailed reasons for some deviations from the B3LYP/TZ values for t_h and t_e will be explained in the next section. The transition dipoles in Table XII are obtained from the area under the observed dielectric function according to Eqs. (7) and (8) and visual inspection of the agreement between calculated and observed line shapes.

From simple arguments relying on a parallel plate condensator with opposite charges on both plates, it is expected that the CT energy depends linearly on the stacking vector.[14] However, as the HOMO-LUMO transition energy in the diimides depends weakly on the type of side group, it is suitable to subtract the reference value E_{00}^{F} before analyzing E_{00}^{CT}. As visualized in Fig. 12, the difference $\Delta_{00}=E_{00}^{\mathrm{CT}}-E_{00}^{\mathrm{F}}$ is a monotonous function of the length of the stacking vector $\mathbf{a}$. Excluding PTCDA, for the other perylene pigments this energy difference follows a linear slope of about $\partial(E_{00}^{\mathrm{CT}}-E_{00}^{\mathrm{F}})/\partial a \approx 0.06$ eV/Å. Some scatter of this difference around a linear dependence on the lattice vector may arise from different values for the effective dielectric function along the stacking vector. For PTCDA, the presence of the anhydride groups induces stronger hydrogen bridges between adjacent molecules and larger quadrupole moments of each molecule. Albeit, it remains unclear how the increased intermolecular interactions determine the deviation of the CT energy from the trend observed in the other perylene compounds.
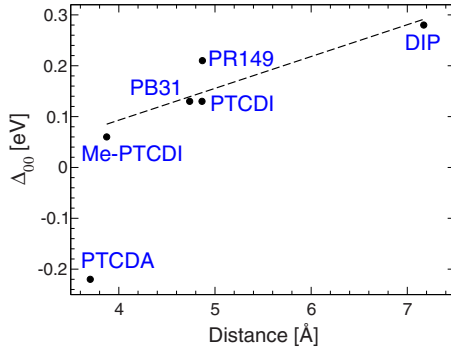
FIG. 12. (Color online) Dependence of the difference Δ_{00} $=E_{00}^{CT}-E_{00}^{F}$ between the lowest vibronic subband of the CT transition and of the neutral molecular excitation on the stacking vector of the six perylene compounds, together with a linear slope fitted through the values of all compounds except for PTCDA.

VIII. CALCULATED LINE SHAPES

In this section, we compare the calculated dielectric tensor elements with ellipsometry spectra or with a Kramers-Kronig consistent analysis of published experimental data as described in Sec. VI.

A. PTCDA

Previous optical studies of PTCDA have shown that Frenkel excitons and CT states mix only weakly, so that they result in quite different features in photoluminescence,[21,27,28] an interpretation corroborated by the small values of the transfer parameters t_e and t_h. PTCDA is one of the exceptional cases where information on the anisotropy of the optical response is available,[22,61] and in contrast to DIP,[32] the large angle between the transition dipoles of the two basis molecules yields oscillator strengths of similar size for both components of the dielectric tensor; compare Tables V and VI. Therefore, it is particularly interesting to analyze the impact of the relatively small mixing between Frenkel and CT states onto the optical response of this model compound. Applying second-order perturbation theory to the small off-diagonal matrix elements according to Eqs. (39)–(42), we find that t_e and t_h produce shifts of the Frenkel exciton transitions below 0.03 eV, so that the parameters of a pure Frenkel model as given in Table XI should remain reliable up to small modifications in the same range.

In Figs. 13 and 14, we present the best fits of the revised analysis of earlier ellipsometry investigations.[22,61,68] Both for ϵ_{xx} and ϵ_{yy}, the calculation reproduces the key features appearing in the experimental spectra, including in each case position and relative height of the lowest vibronic subband and the main band at about 2.5 eV. The transition dipoles from Table XII used in the calculated line shapes are close to the TD-DFT value of 6.93 D; compare Table X. Small deviations between the chosen transition dipoles can be related to an energy-dependent slope contained in the observed data which may arise from unknown contributions such as non-specular diffuse reflection, so that the data analysis of spectroscopic ellipsometry gives a small positive value $\Im(\epsilon)$ in
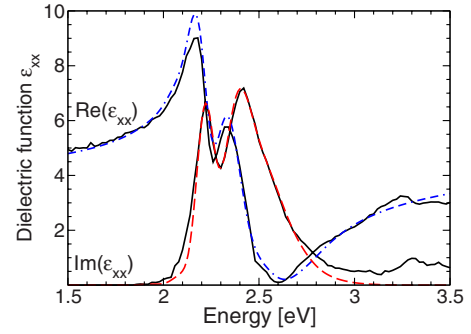
FIG. 13. (Color online) Comparison of model calculation (red dashed, blue dash-dotted) with revised values of the dielectric tensor element ϵ_{xx} (black), obtained from a (102) face of a single crystal of α-PTCDA, with the plane of incidence perpendicular to the **b** lattice vector (Ref. 61).

specific energetic regions where no Frenkel or CT transitions are expected, e.g., around 3 eV.

In the full F-CT model, the F-CT mixing shifts the lowest transitions by a few meV below $E_{00}^{CT}=1.95$ eV; compare Figs. 13 and 14. The dipolar coupling strength of these transitions arises mainly from the small CT transition dipole obtained from TD-DFT, so that it remains much smaller than the strength of transitions at higher energy dominated by the large transition dipole of neutral excitations. Even though these tiny calculated absorption features are hardly visible in Figs. 13 and 14, recent PL excitation studies have demonstrated that excitation in this energetic region can selectively produce PL from CT states confirming that our value of E_{00}^{CT} is realistic.[65] Moreover, at room temperature, in the region around the first excited vibronic level of the CT transition at $E_{01}^{CT}=E_{00}^{CT}+\hbar\omega=2.12$ eV, PL excitation spectra show a resonance allowing selective excitation of PL from excimers,[9,65] a further indication that weakly absorbing CT transitions play a key role for the excitation of PL from self-trapped CT excitons.

Using the parameters for the pure Frenkel excitons according to the sum rules discussed in Sec. VI and Table XI, the agreement with the observed dielectric tensor deteriorates significantly; compare Figs. 15 and 16. Therefore, although in PTCDA the mixing between Frenkel and CT states is particularly small, the adjustment of E_{00}^{CT} with respect to E_{00}^{F} in
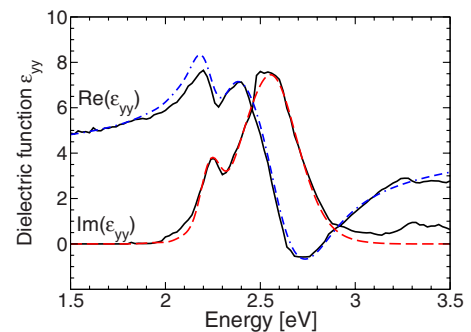
FIG. 14. (Color online) As in Fig. 13, but for tensor element ϵ_{yy}, obtained with plane of incidence parallel to the **b** lattice vector (Ref. 61).
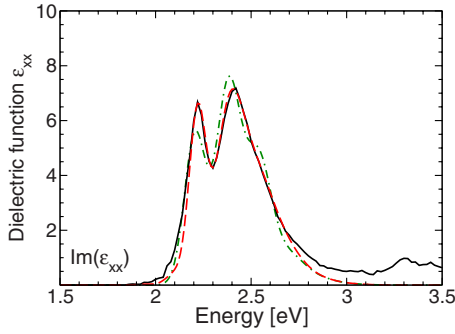
FIG. 15. (Color online) Revised dielectric tensor element $\Im(\epsilon_{xx})$ (Ref. 61), and calculated line shapes relying either on the full F-CT model (red dashed), or exclusively on Frenkel excitons (green dash-dotted), with parameters according to Tables XII and XI, respectively.

the full F-CT model still improves the calculated shapes for both elements of the dielectric tensor. The sensitivity of the calculated line shape on the energetic difference $E_{00}^{CT} - E_{00}^{F}$ is visualized in Fig. 17, where $E_{00}^{F} = 2.17$ eV was kept fixed, but E_{00}^{CT} was modified by ± 0.07 eV. From the significant deviation between the calculated line shapes for $\Im(\epsilon_{xx})$ and the observed data we conclude that our exciton model allows to determine the CT energy within an uncertainty range of $E_{00}^{CT} = 1.95 \pm 0.07$ eV, or less than half of the effective internal vibration.

In summary, for PTCDA, the availability of the anisotropic dielectric tensor allows to deduce the parameters for transfer of neutral excitations $T_{AA}(\mathbf{0})$ and $T_{AB}(\mathbf{0})$ in a model relying exclusively on Frenkel excitons. In a second step, a refined model including the mixing between Frenkel excitons and CT states determines the energetic position of the CT transition within a precision of better than 0.07 eV resulting in a remarkable agreement between calculated and measured anisotropy of the dielectric tensor. Due to the smallness of electron transfer t_e and hole transfer t_h, the full model does not require large changes of the Frenkel parameters determined beforehand.

PTCDA seems to be the only perylene compound where the CT transition E_{00}^{CT} is placed significantly below the neutral excitation of a molecule in the crystalline phase, E_{00}^{F}. Therefore, PL bands arising from self-trapped CT states occur below recombination from the dispersion minimum of the lowest dispersion branch of the Frenkel exciton,
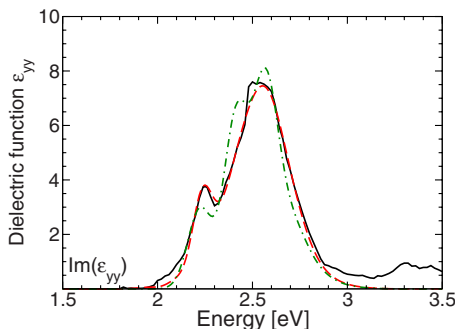
FIG. 16. (Color online) As in Fig. 15, but for ϵ_{yy}.
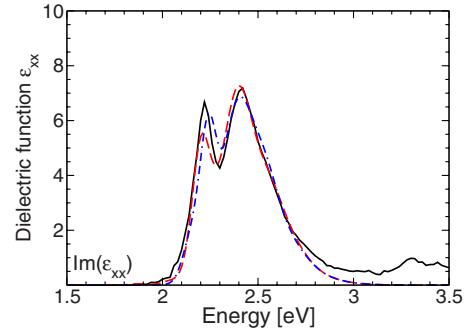
FIG. 17. (Color online) As in Fig. 13, but calculated with $E_{00}^{CT} = 1.88$ eV (red dashed) and $E_{00}^{CT} = 2.02$ eV (blue dash-dotted).

$E_{00}^{F}(\mathbf{k})$.[21,27,28] Moreover, weak transitions around 1.95 eV and 2.12 eV arising from E_{00}^{CT} and E_{01}^{CT}, respectively, allow the selective excitation of PL from CT states.[9,65] The value of $E_{00}^{CT} = 1.95 \pm 0.07$ eV deduced from the Frenkel-CT model corresponds to an average CT transition energy of $\langle E^{CT} \rangle = E_{00}^{CT} + (S_+ + S_-)\hbar\omega = 2.12 \pm 0.07$ eV, in good agreement with an earlier estimate based on excimer PL arising from a self-trapped CT exciton modeled as a deformed dimer, indicating a value in the range $\langle E^{CT} \rangle = 2.14 \pm 0.08$ eV for the undeformed crystal.[28]

B. Me-PTCDI

Among the six compounds studied, Me-PTCDI has the largest electron transfer parameter t_e, so that the calculated line shape $\Im(\epsilon_{yy})$ in Fig. 11 obtained from a pure Frenkel exciton model deviates strongly from the reference curve deduced from the experimental observations. The particularly large energetic difference between the strongest observed features at about 2.12 and 2.5 eV indicates that the charge transfer breaks the entire line shape into two well separated bands, with some weaker features in between. We found empirically that the B3LYP/TZ values of $t_e = -0.104$ eV and $t_h = -0.041$ eV are slightly too large in absolute size, irrespective of the position of the CT transition E_{00}^{CT}.

As shown in Fig. 18, slightly smaller parameters for elec-
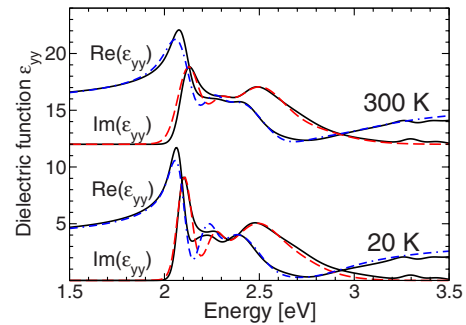
FIG. 18. (Color online) Model calculation of dielectric tensor element ϵ_{yy} (red dashed, blue dash-dotted) superimposed to the dielectric function deduced from optical density and reflectivity (Ref. 11) (solid lines); compare Fig. 10 for $T = 300$ K. For clarity, the curves for room temperature are shifted upward, with a baseline of 12.

tron transfer of $t_e = -0.090$ eV and hole transfer of $t_h = -0.020$ eV provide a line shape in good agreement with the experimental curve when Frenkel and CT transitions are close to degenerate, $\Delta_{00} = E_{00}^{CT} - E_{00}^F = 0.06$ eV. From Eqs. (30)–(33) and Eq. (42), it can be deduced that at $\mathbf{k} = \mathbf{0}$, the off-diagonal matrix element between these two transitions is determined by the sum $t_h' + t_e'$. The deformation parameters in Table III together with $t_e = -0.090$ eV and $t_h = -0.020$ eV yield $t_e' = t_e S_{0_e 0_+} S_{0_g 0_-} = -0.062$ eV and $t_h' = t_h S_{0_e 0_-} S_{0_g 0_+} = -0.017$ eV, or $t_h' + t_e' = -0.079$ eV. In contrast to the simpler Frenkel exciton model, the lowest observed subband is no more placed slightly above the lowest molecular transition E_{00}^F. Instead, the particularly large interaction between Frenkel and CT manifold pushes it to 0.08 eV below E_{00}^F, but it still derives the main part of its oscillator strength from this molecular transition. According to the sum rule Eq. (50), the increase in E_{00}^F by 0.13 eV with respect to the value estimated in the pure Frenkel model corresponds to a reduction in $T_{AA}(\mathbf{0})$ by a similar amount, so that the F-CT model is now based on a much smaller exciton transfer parameter $T_{AA}(\mathbf{0}) = 0.08$ eV. Therefore, Me-PTCDI can serve as a prototype for a material where the mixing between Frenkel and CT states has the largest influence on the line shape of the optical response, as opposed to PTCDA, where the transfer of neutral excitations represents the most important intermolecular interaction.

The transition dipole $\mu_F = 5.98$ D used for the calculated line shape is below a previous experimental estimate of 6.8 ± 0.7 D (Ref. 18) and our TD-DFT value of 7.42 D; compare Tables X and XII. Such a rather large deviation indicates a questionable absolute scale of the reflectivity and optical density underlying our experimental model lines shape of ϵ_{yy},[11] compare Sec. V for details of the data analysis.

In the region of the first valley in the imaginary part of the dielectric function around 2.2 eV, the exciton model cannot provide an optical response of similar size. At the present stage, we do not know if this reveals a principal limitation of our approach or contributions from a slightly different crystal phase to the measured spectra, e.g., based on different orientations of the methyl groups.[69]

Similarly to the opposite limit of very small electron and hole transfer parameters realized for PTCDA, the position of the lowest CT transition can be determined quite accurately. In Fig. 19, the deviation of the calculated spectra from the experimental reference curve obtained for variations in the CT energy by ± 0.05 eV demonstrates that an uncertainty range of $E_{00}^{CT} = 2.24 \pm 0.05$ eV at low temperature or $E_{00}^{CT} = 2.26 \pm 0.05$ eV at room temperature is a conservative estimate.

Recently, Kramers-Kronig consistent values for the dielectric function of polycrystalline Me-PTCDI films have been derived from spectroscopic ellipsometry.[70] Our exciton model can reproduce these observations, but the calculation requires transition energies which are blueshifted by 0.02 eV with respect to previous measurements of the optical density at room temperature reported in the present work.[11] The small differences in the energetic positions of the dielectric response indicate an influence of strain on the optical observables of thin films grown under different conditions.[11,70]
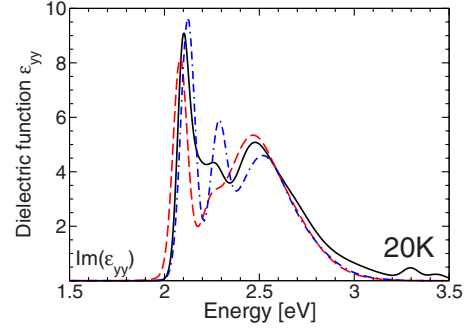
FIG. 19. (Color online) Calculated model line shapes for Me-PTCDI obtained with modified CT energies: $E_{00}^{CT} = 2.19$ eV (red dashed) and $E_{00}^{CT} = 2.29$ eV (blue dash-dotted) superimposed to $\Im(\epsilon_{yy})$ at $T = 20$ K (black).

C. PB31

The spectrum of PB31 resembles the one of Me-PTCDI, but in PB31, the very large splitting between the two strongest features at 2.01 and 2.64 eV is realized by an extraordinarily large hole transfer parameter interfering constructively with a somewhat smaller electron transfer. In contrast to Me-PTCDI, the relatively large angle between the two long axes of the two basis molecules in the PB31 unit cell assigns substantial coupling strengths both to ϵ_{xx} and to ϵ_{yy}; compare Table V. The published data for the optical density were measured on polycrystalline films, so that both diagonal elements of the calculated dielectric tensor have to be averaged.

Based on the values $t_h = 0.144$ eV and $t_e = 0.053$ eV, the latter slightly reduced with respect to the B3LYP/TZ reference, our model can reproduce the experimental line shape quite well; compare Fig. 20. Together with the deformation parameters from Table III, we obtain $t_h' = 0.131$ eV and $t_e' = 0.034$ eV, interfering constructively as $t_h' + t_e' = 0.165$ eV in the off-diagonal matrix element between E_{00}^{CT} and E_{00}^F. Therefore, the lowest subband contributing to the dielectric function has again mixed Frenkel-CT character. The resulting line shape of the average between ϵ_{xx} and to ϵ_{yy} is visualized in Fig. 20 reproducing all details of the experimental reference. The best agreement with the experimental line shape is found if the CT transitions are significantly above the neutral excitations, with a difference of $E_{00}^{CT} - E_{00}^F = 0.13$ eV. From modi-
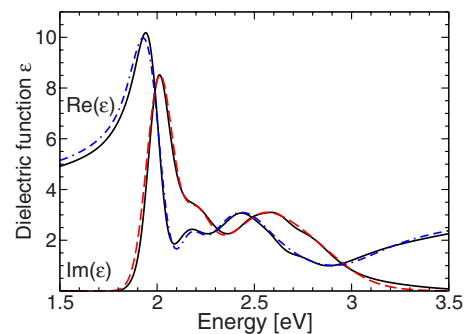
FIG. 20. (Color online) Comparison of calculated dielectric function $\epsilon_\| = (\epsilon_{xx} + \epsilon_{yy})/2$ of PB31 (red dashed, blue dash-dotted) to Kramers-Kronig consistent fit of measured data obtained at $T = 12$ K (black) (Ref. 11).
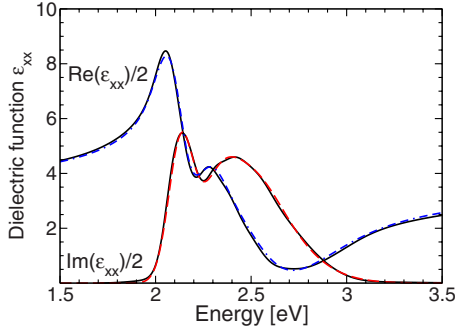
FIG. 21. (Color online) Comparison of the calculated dielectric function of PTCDI (red dashed, blue dash-dotted) with reference curves (black) obtained from the measured absorbance (Ref. 62).

fied values for the CT transition, we deduce again an uncertainty range of ± 0.05 eV for E_{00}^{CT}. The transition dipole of $\mu_F = 10.38$ D underlying the calculated line shape deviates rather strongly from the TD-DFT reference of $\mu_F = 8.62$ D in Table XII presumably due to a problem in the determination of the measured film thickness of 100 nm underlying our data analysis.[11] The black color of PB31 is a direct consequence of the exceptionally large contribution of $t_e + t_h$ to the second moment of $\Im(\epsilon)$ according to Eq. (53), so that this material absorbs over a quite wide energetic region covering the entire visible range of the spectrum.

D. PTCDI

The optical absorbance of PTCDI shows a fairly large broadening of the lowest subband with a full width at half maximum corresponding roughly to the energy of the calculated effective internal mode of 0.175 eV, compare Table III,[62] indicating rather large elongations of external librational phonons after optical excitation.

As shown in Fig. 21, we found the best agreement with the measured line shape when using $t_h = 0.076$ eV and $t_e = 0.019$ eV, where the larger parameter is somewhat smaller than the B3LYP/TZ reference. Due to the constructive interference of these transfer parameters, the off-diagonal matrix element between E_{00}^{CT} and E_{00}^{F} is still as large as $t_h' + t_e' = 0.079$ eV. In absolute, this matrix element is of similar size as in Me-PTCDI, but the larger splitting of $E_{00}^{CT} - E_{00}^{F} = 0.13$ eV reduces the influence of F-CT interaction onto the relative strength of adjacent vibrational subbands. Moreover, the larger broadening does not allow to resolve distinct features in the valley region between the two main bands.

E. PR149

Using parameters rather close to the B3LYP/TZ values for electron transfer and hole transfer, the agreement of the model calculation in Fig. 22 with the dielectric function deduced from experimental data is fairly good, but the shape of the lowest vibronic subband cannot be reproduced quantitatively. This failure might indicate that charge transfer between the two basis molecules results in a substantial redistribution of oscillator strength between the lowest two subbands, an interaction mechanism not included in our ap-
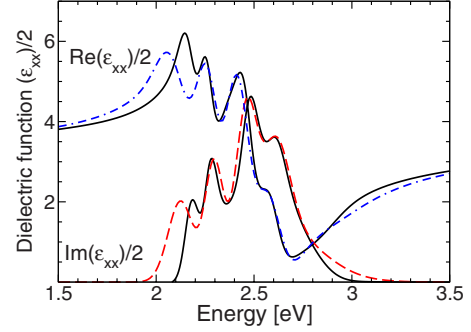
FIG. 22. (Color online) Model calculation of the dielectric function $\epsilon_{xx}/2$ of PR149 (red dashed, blue dash-dotted) determining the optical density of polycrystalline thin films superimposed to a Kramers-Kronig consistent dielectric function fitted to the published optical density (Ref. 11). The background of the real part of the dielectric function was assumed to correspond to Me-PTCDI.

proach. A model calculation with modified Huang-Rhys factors can improve on this situation, but we do not think such modified parameters can still have a sound microscopic foundation. Instead, from the TD-DFT results of the stacked dimer, we found that other low-lying dipole-active transitions occur rather close to the HOMO-LUMO transition. Therefore, it seems that a more complicated exciton model based on several molecular transitions would be required in order to improve the agreement between calculated and measured line shapes.

F. DIP

Since the geometric overlap between adjacent DIP molecules in the thin film phase is almost negligible, in keeping with a quite large stacking vector of $a = 7.17$ Å, all intermolecular parameters are particularly small; compare Tables VII and XII. The largest element of the observed dielectric tensor shown in Fig. 23 resembles a vibronic progression with a Huang-Rhys factor around $S = 1$. As discussed elsewhere in more detail, a pure Frenkel model cannot reproduce the ob-
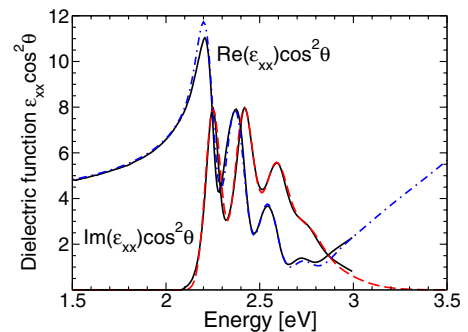
FIG. 23. (Color online) Model calculation of the out-of-plane dielectric function for DIP in its thin film phase (red dashed, blue dash-dotted), superimposed to the respective element of the dielectric tensor determined from spectroscopic ellipsometry (black).[32] In the calculated curves, the tilting of the long axis of the DIP molecules against the substrate normal by $\theta = 19.8^0$ has been included through a reduction factor of $\cos^2 \theta$.

served dielectric function, so that the mixing of Frenkel and CT states via the small values for electron and hole transfer is required for an interpretation of the observed line shape.[32] In the present work, the effective mode underlying the calculated line shape is determined from DFT in contrast to an effective mode fitted to solution spectra used earlier.[32] Moreover, we found that in the previous calculation based on the same Frenkel-CT model, we have used the wrong sign for the hole transfer. Now, with values of $t_e = -0.033$ eV and $t_h = -0.056$ eV close to the B3LYP/TZ reference, the agreement between calculated and measured line shape improves significantly; compare Fig. 23.

IX. CONCLUSION

In the present work, we have demonstrated that an exciton model accounting for the interference between Frenkel excitons and charge-transfer transitions can quantitatively reproduce the observed optical spectra of several perylene compounds. These model calculations rely on internal molecular deformations of excited or charged molecules obtained with DFT and intermolecular electron and hole transfer along the stacking direction close to the respective values deduced from DFT and Hartree-Fock. In a subsequent parametrization step addressing exclusively Frenkel excitons, a reasonable range for the energy of the lowest molecular transition and for the transfer of neutral excitations can be obtained from a sum rule applied to the observed dielectric function. For compounds with relatively small electron and hole transfer such as PTCDA and DIP, the small mixing of Frenkel and CT states results only in marginal modifications of the neu-

tral molecular excitation energy and the respective transfer matrix elements derived from the sum rule. In the opposite limit of strong mixing of Frenkel and CT features realized in the other four perylene compounds studied, the complete exciton model is required for quantifying the nontrivial progression over the various vibronic subbands, and the preliminary parameters obtained in the Frenkel model are subject to substantial modifications. A new sum rule for the second moment of the observed line shape can be applied to measured data in order to assess the importance of the interference between Frenkel excitons and CT states via electron or hole transfer.

For materials with large electron or hole transfer, the exciton model allows to determine the energies of CT transitions along the stacking direction within a precision better than 0.05 eV, an uncertainty range far below systematic deviations occurring in HF, DFT, or microelectrostatic calculations. In the future, these improved values for the CT energies should allow a deeper understanding of device-related observables such as photocurrents and a refinement of existing microscopic models for photoluminescence.

*linus.gisslen@ph.tum.de

†reinhard.scholz@wsi.tum.de

[1] W. Herbst and K. Hunger, *Industrial Organic Pigments* (Wiley-VCH, Berlin, 2005).

[2] E. Hädicke and F. Graser, Acta Crystallogr. C **42**, 189 (1986); **42**, 195 (1986).

[3] K. Sato, J. Mizuguchi, Y. Sakai, and S. Aramaki, J. Appl. Phys. **103**, 013702 (2008).

[4] K. Hirao, Y. Tsukada, S. Suzuki, H. Takahashi, and J. Mizuguchi, J. Appl. Phys. **103**, 053706 (2008).

[5] C. Li, J. Yum, S. Moon, A. Herrmann, F. Eickemeyer, N. Pschirer, P. Erk, J. Schöneboom, K. Müllen, M. Grätzel, and M. Nazeeruddin, ChemSusChem **1**, 615 (2008).

[6] J. Mizuguchi, J. Appl. Phys. **84**, 4479 (1998).

[7] K.-Y. Law, Chem. Rev. **93**, 449 (1993).

[8] Z. Shen, P. E. Burrows, V. Bulović, and S. R. Forrest, Science **276**, 2009 (1997).

[9] V. Bulović, P. E. Burrows, S. R. Forrest, J. A. Cronin, and M. E. Thompson, Chem. Phys. **210**, 1 (1996).

[10] U. Gómez, M. Leonhardt, H. Port, and H. C. Wolf, Chem. Phys. Lett. **268**, 1 (1997).

[11] J. Mizuguchi and K. Tojo, J. Phys. Chem. B **106**, 767 (2002).

[12] E. Engel, K. Schmidt, D. Beljonne, J.-L. Brédas, J. Assa, H. Fröb, K. Leo, and M. Hoffmann, Phys. Rev. B **73**, 245216

(2006).

[13] G. Klebe, F. Graser, E. Hädicke, and J. Berndt, Acta Crystallogr. B **45**, 69 (1989).

[14] P. M. Kazmaier and R. Hoffmann, J. Am. Chem. Soc. **116**, 9684 (1994).

[15] A. S. Davydov, *Theory of Molecular Excitons* (Plenum Press, New York, 1971).

[16] Z. G. Soos, M. H. Hennessy, and G. Wen, Chem. Phys. **227**, 19 (1998).

[17] M. H. Hennessy, Z. G. Soos, R. A. Pascal, and A. Girlando, Chem. Phys. **245**, 199 (1999).

[18] M. Hoffmann, K. Schmidt, T. Fritz, T. Hasche, V. M. Agranovich, and K. Leo, Chem. Phys. **258**, 73 (2000).

[19] M. Hoffmann and Z. G. Soos, Phys. Rev. B **66**, 024305 (2002).

[20] I. Vragović, R. Scholz, and M. Schreiber, Europhys. Lett. **57**, 288 (2002).

[21] I. Vragović and R. Scholz, Phys. Rev. B **68**, 155202 (2003).

[22] M. I. Alonso, M. Garriga, N. Karl, J. O. Ossó, and F. Schreiber, Org. Electron. **3**, 23 (2002).

[23] G. Mazur, P. Petelenz, and M. Slawik, J. Chem. Phys. **118**, 1423 (2003).

[24] R. Fulton and M. Gouterman, J. Chem. Phys. **41**, 2280 (1964).

[25] J. S. Briggs and A. Herzenberg, Proc. Phys. Soc. **92**, 159 (1967).

[26] J. S. Briggs and A. Herzenberg, J. Phys. B **3**, 1663 (1970).

[27] A. Yu. Kobitski, R. Scholz, D. R. T. Zahn, and H. P. Wagner, Phys. Rev. B **68**, 155201 (2003).

[28] R. Scholz, A. Y. Kobitski, D. R. T. Zahn, and M. Schreiber, Phys. Rev. B **72**, 245208 (2005).

[29] R. Scholz, I. Vragović, A. Yu. Kobitski, M. Schreiber, H. P. Wagner, and D. R. T. Zahn, Phys. Status Solidi B **234**, 402 (2002).

[30] M. Knupfer, T. Schwieger, J. Fink, K. Leo, and M. Hoffmann, Phys. Rev. B **66**, 035208 (2002).

[31] I. Vragović, R. Scholz, and M. Schreiber, J. Lumin. **110**, 284 (2004).

[32] U. Heinemeyer, R. Scholz, L. Gisslén, M. I. Alonso, J. O. Ossó, M. Garriga, A. Hinderhofer, M. Kytka, S. Kowarik, A. Gerlach, and F. Schreiber, Phys. Rev. B **78**, 085210 (2008).

[33] D. Becke, Phys. Rev. A **38**, 3098 (1988); C. Lee, W. Yang, and R. G. Parr, Phys. Rev. B **37**, 785 (1988).

[34] C. W. Bauschlicher, Chem. Phys. Lett. **246**, 40 (1995).

[35] M. D. Halls, J. Velkovski, and H. B. Schlegel, Theor. Chem. Acc. **105**, 413 (2001).

[36] A. Schäfer, C. Huber, and R. Ahlrichs, J. Chem. Phys. **100**, 5829 (1994).

[37] O. Treutler and R. Ahlrichs, J. Chem. Phys. **102**, 346 (1995).

[38] R. Bauernschmitt and R. Ahlrichs, Chem. Phys. Lett. **256**, 454 (1996).

[39] R. Ahlrichs, M. Bär, M. Häser, H. Horn, and C. Kölmel, Chem. Phys. Lett. **162**, 165 (1989).

[40] P. Hohenberg and W. Kohn, Phys. Rev. **136**, B864 (1964).

[41] K. Akers, R. Aroca, A. M. Hor, and R. O. Loutfy, J. Phys. Chem. **91**, 2954 (1987).

[42] R. Scholz, A. Yu. Kobitski, T. U. Kampen, M. Schreiber, D. R. T. Zahn, G. Jungnickel, M. Elstner, M. Sternberg, and Th. Frauenheim, Phys. Rev. B **61**, 13659 (2000).

[43] K. Akers, R. Aroca, A. M. Hor, and R. O. Loutfy, Spectrochim. Acta, Part A **44**, 1129 (1988).

[44] G. Salvan, S. Silaghi, B. Paez, T. U. Kampen, and D. R. T. Zahn, Appl. Surf. Sci. **234**, 178 (2004).

[45] V. Coropceanu, J. M. André, M. Malagoli, and J. L. Brédas, Theor. Chem. Acc. **110**, 59 (2003).

[46] A. J. Lovinger, S. R. Forrest, M. L. Kaplan, P. H. Schmidt, and T. Venkatesan, J. Appl. Phys. **55**, 476 (1984).

[47] J. Mizuguchi, Acta Crystallogr. C **54**, 1479 (1998).

[48] K. Tojo and J. Mizuguchi, Z. Kristallogr. - New Cryst. Struct. **217**, 45 (2002).

[49] J. Mizuguchi and K. Tojo, Z. Kristallogr. - New Cryst. Struct. **216**, 375 (2001).

[50] M. A. Heinrich, J. Pflaum, A. K. Tripathi, W. Frey, M. L. Steigerwald, and T. Siegrist, J. Phys. Chem. C **111**, 18878 (2007).

[51] M. Möbus, N. Karl, and T. Kobayashi, J. Cryst. Growth **116**, 495 (1992).

[52] H. Yamane, S. Kera, K. K. Okudaira, D. Yoshimura, K. Seki, and N. Ueno, Phys. Rev. B **68**, 033102 (2003).

[53] G. N. Gavrila, H. Mendez, T. U. Kampen, D. R. T. Zahn, D. V. Vyalikh, and W. Braun, Appl. Phys. Lett. **85**, 4657 (2004).

[54] I. G. Hill, A. Kahn, Z. G. Soos, and R. A. Pascal, Chem. Phys. Lett. **327**, 181 (2000).

[55] E. V. Tsiper and Z. G. Soos, Phys. Rev. B **64**, 195124 (2001).

[56] E. V. Tsiper, Z. G. Soos, W. Gao, and A. Kahn, Chem. Phys. Lett. **360**, 47 (2002).

[57] M. Wewer and F. Stienkemeier, J. Chem. Phys. **120**, 1239 (2004).

[58] A. Dreuw, J. L. Weisman, and M. Head-Gordon, J. Chem. Phys. **119**, 2943 (2003).

[59] Y. C. Cheng, R. J. Silbey, D. A. da Silva Filho, J. P. Calbert, J. Cornil, and J. L. Brédas, J. Chem. Phys. **118**, 3764 (2003).

[60] C. Kittel, *Quantum Theory of Solids* (Wiley, New York, 1963).

[61] M. I. Alonso M. Garriga, J. O. Ossó, F. Schreiber, and R. Scholz, revised evaluation of ellipsometry spectra of PTCDA (unpublished).

[62] S. Tokito, J. Sakata, and Y. Taga, J. Appl. Phys. **77**, 1985 (1995).

[63] B. Krause, A. C. Dürr, F. Schreiber, H. Dosch, and O. H. Seeck, J. Chem. Phys. **119**, 3429 (2003).

[64] V. R. Gangilenka, A. De Silva, H. P. Wagner, R. E. Tallman, B. A. Weinstein, and R. Scholz, Phys. Rev. B **77**, 115206 (2008).

[65] V. R. Gangilenka, L. V. Titova, L. M. Smith, H. P. Wagner, L. A. A. De Silva, and R. Scholz (unpublished).

[66] H. P. Wagner, V. R. Gangilenka, A. DeSilva, H. Schmitzer, R. Scholz, and T. U. Kampen, Phys. Rev. B **73**, 125323 (2006).

[67] A. Djurišić, T. Fritz, and K. Leo, Opt. Commun. **183**, 123 (2000).

[68] M. I. Alonso and M. Garriga, Thin Solid Films **455-456**, 124 (2004).

[69] CSD (Cambridge structural database) file for Me-PTCDI corresponding to Ref. 2.

[70] D. Lehmann and D. R. T. Zahn, Appl. Phys. A: Mater. Sci. Process. **95**, 203 (2009).